CryoTEMPO-EOLIS

Elevation Over Land Ice from Swath Algorithm Theoretical Basis Document

Land Ice Elevation Thematic Point Product

Land Ice Elevation Thematic Gridded Product

Issue: 3.1

Date: 22nd June 2026

Approval

Name	Date	Signed
Alessandro Di Bella ESA		
Noel Gourmelen University of Edinburgh		
Livia Jakob Earthwave		

Document Versions

Issue	Date	Reason for change
1.0	8th November 2021	First version of document
1.1	29th December 2021	Updated and reviewed
2.0	5th September 2022	Updated for CryoTEMPO EOLIS Baseline 2
2.1	15th March 2023	Updated for release of CryoTEMPO-EOLIS Baseline 2
2.2	22nd January 2024	Updated for the release of new products
2.3	13th May 2024	Updated to include the new Antarctic Ice Shelves product
3.0	24th January 2026	Updated for CryoTEMPO EOLIS Baseline 3
3.1	22nd June 2026	Updated to reflect operational seamless product algorithm

Contents

List of acronyms

CLI	CryoTEMPO Land Ice
DEM	Digital Elevation Model
EO	Earth Observation
EOLIS	Elevation Over Land Ice from Swath
ESA	European Space Agency
FTP	File Transfer Protocol
GS	Ground Segment
LRM	Low Resolution Mode
NetCDF	Network Common Data Form (binary file format)
OIB	Operation Ice Bridge
PDGS	Payload Download Ground Segment
POCA	Point-Of-Closest-Approach
SARIn	Synthetic Aperture Radar Interferometric
STSE	Support To Science Element
UoE	University of Edinburgh
UTC	Coordinated Universal Time
XML	Extensible Mark-up Language

1 Introduction

1.1 Purpose and Scope

This document contains the Algorithm Theoretical Basis for the ESA CryoTEMPO-EOLIS project. The ATBD describes the scientific background and principle of the algorithms, their expected or known accuracy and performance, the input and output data, as well as capabilities and limitations.

1.2 Reference Websites

CryoTEMPO-EOLIS Project Website: http://cryotempo-eolis.org/

CryoTOP Evolution: https://cryotop-evolution.org/

CryoSat + Mountain Glaciers: http://www.cryosat-mtg.org/

ESA CryoSat-2 Data Download: https://science-pds.cryosat.esa.int/

Operation IceBridge: https://nsidc.org/data/icebridge/

Arctic DEM: https://www.pgc.umn.edu/data/arcticdem/

REMA DEM: https://www.pgc.umn.edu/data/rema/

Gapless-REMA100: https://figshare.com/articles/dataset/Gapless-REMA100/19122212

SRTM DEM: https://srtm.csi.cgiar.org/

Copernicus DEM: https://registry.opendata.aws/copernicus-dem

ICESat-2: https://icesat-2.gsfc.nasa.gov/

Randolph Glacier Inventory (RGI) 7.0: https://glims-rgi.github.io/rgi_user_guide/welcome.html

MEaSUREs BedMachine: https://nsidc.org/data/nsidc-0756/versions/3

Polar+Iceshelves: https://polar-iceshelf.org

CryoTEMPO Land Ice: http://www.cpom.ucl.ac.uk/cryotempo/about.php?theme=landice

PolarGap: https://earth.esa.int/eogateway/campaigns/polargap

2 Scientific Background

Global ice loss has been increasing over the past decades, with large contributions from glaciers, as well as from the two ice sheets (Slater, et al., 2021). Global and continuous monitoring of these environments however remains a challenging task, with estimates relying on a variety of observations and models to achieve the required spatial and temporal coverage.

CryoSat-2 is the first altimeter to carry a SAR interferometer, which allows a sharper footprint and the ability to precisely locate the position of the ground echo (Wingham, Phalippou, Mavrocordatos, & Wallis, 2004). In practice, CryoSat's revolutionary interferometric design has allowed several technical breakthroughs and led to the application of radar altimetry to environments that were previously unforeseen. The conventional method of processing CryoSat-2 waveforms measures surface elevations at the Point-Of-Closest-Approach (POCA), sampling one elevation measurement per waveform at the closest point on the Earth's surface beneath the satellite. In contrast, the novel swath processing technique extracts multiple elevation measurements across the waveform, increasing the data volume and improving spatial as well as temporal coverage, enabling the use of CryoSat-2 measurements in new environments such as on mountain glaciers (Gourmelen, et al., 2018).

Following on from the early demonstration of the technique and its potential impact, the "CryoSat ThEMatic PrOducts – SWATH Cryo-TEMPO" project (CryoTEMPO-EOLIS) consolidates the research and development undertaken during the CryoSat+ CryoTop / CryoTop evolution ESA STSE projects (Gourmelen, et al., 2018),the CryoSat+ Mountain Glaciers project (Foresta, et al., 2016; Foresta, et al., 2018; Jakob L. , Gourmelen, Ewart, & Plummer, 2021; Jakob & Gourmelen, 2023) and Polar+ Ice Shelves project (Gourmelen, et al., 2017; Davison, et al., 2023) into operational products. The purpose of the thematic products is to make the data available to the wider scientific community in a form that does not require a detailed understanding of the sensor used and extensive processing. This product allows users to perform analysis using swath data, and provides an uncertainty metric on which to filter the data to a desired precision.

3 The EOLIS Products

CryoTEMPO-EOLIS consists of three distinct products:

1) **Monthly Point product:**
    - Containing elevation point measurements with an associated uncertainty
    - The point product covers the two ice sheets (Antarctic Ice Sheet and Greenland Ice Sheet) as defined by the 'land_ice' surface type in BedMachine V3 / V5 (Morlighem, et al., 2020) (Morlighem M. , 2022) (Morlighem M. e., 2022), the Antarctic Ice Shelves as defined by the 'floating_ice' surface type in MEaSUREs BedMachine V3 (Morlighem, et al., 2020) (Morlighem M. , 2022) and the glacier regions, as defined by RGI 7.0 (RGI 7.0 Consortium, 2023). The glacier regions include Iceland, Svalbard, Arctic Canada, Russian Arctic, Alaska, Southern Andes, High Mountain Asia, Western Canada & USA, Scandinavia, Central Europe, Low Latitudes, New Zealand, the peripheral glaciers in Antarctica and the peripheral glaciers in Greenland.
    - It is described in further detail in Section 4

2) **Monthly gridded product:**
    - Containing a spatial interpolation of the point product onto a uniform grid of elevations and elevation changes, and their corresponding uncertainties
    - The monthly gridded product covers a subset of the point product regions with the highest coverage: Greenland Ice Sheet and Peripheral Glaciers, Antarctic Ice Sheet and Peripheral Glaciers, Iceland, Svalbard, Russian Arctic, Arctic Canada and Southern Andes.
    - It is described in further detail in Sections 5.1 and 5.2

3) **Annual gridded product**
    - Containing a seamless, uniform grid of elevations and their corresponding uncertainties.
    - The seamless annual gridded product covers the Antarctic and Greenland Ice Sheets, and the Antarctic Ice Shelves.
    - It is described in further detail in Section 5.3

Figure 1: Coverage of point and gridded products in CryoTEMPO-EOLIS

3.1 Processing Overview

The processing chain to generate the thematic products consists of multiple phases. The diagram in Figure 2 illustrates the sequence of steps in the processing chain.

Figure 2: CryoTEMPO-EOLIS Processing Chain Sequence.

The swath generation as described in (Gourmelen, et al., 2018) uses the along track L1B files and a reference DEM to compute a set of points perpendicular to the satellite's track referred to as the swath points. The data ingestion phase builds a spatial and temporal index of the along track data into 100 x 100 km tiles. The uncertainty value for a given point of data is computed using these tiles.

The Level 2 Baseline E NetCDF feed is used to source the POCA data that is ingested and included in the EOLIS point and gridded products. The columns used are: *height_1_20_ku* for the elevations, *retracker_1_quality_20_ku* for retracker quality filtering*, lat_poca_20_ku* and *lon_poca_20_ku* for position. The ESA CryoSat Product Handbook contains definitions of the column names (ESA, 2019).

The latitude and longitude coordinates are transformed to a local coordinate system using a consistent projection with the swath point data (see Table 1). The difference of POCA elevation to the reference DEM is used as a filter for erroneous data excluding any POCA points that are greater than 150m in difference from a reference DEM. The POCA data is also filtered on *retracker_1_quality_20_ku,* excluding points with a retracker quality metric equal to 0. These points are excluded because they correspond to locations where the retracker has failed, and the point position that has been recorded has defaulted to nadir.

4 Point Products

The CryoTEMPO-EOLIS point product is a set of high quality CryoSat-2 swath altimetry point data with uncertainty metrics applied. This product is designed to be user-friendly, so that it can be used by non-altimetry experts. The point products cover the following regions: Antarctic and Greenland Ice Sheets and peripheral glaciers, Antarctic Ice Shelves, as well as the ice caps and glaciers in Iceland, Svalbard, Alaska, Arctic Canada, Russian Arctic, Southern Andes, High Mountain Asia, Western Canada & USA, Scandinavia, Central Europe, Low Latitudes and New Zealand (see). The definition of these regions follows the BedMachine definition of the Greenland and Antarctic Ice sheet, and Antarctic Ice Shelves, and the RGI 7.0 definition of the glacier areas.

4.1 Point Product Input Data

4.1.1 Reference DEMs

Different reference DEMs are used in different regions: Table 1 provides a summary of this. Overall, 3 DEMs are used: the Arctic DEM v4.1 mosaic (Porter, et al., 2018), REMA DEM v2 (Howat, 2022), and Copernicus GLO-30 (European Space Agency; Sinergise, 2021).

Table 1: Choice of reference DEM used for each EOLIS region

EOLIS Region	Reference DEM
Alaska	Copernicus GLO-30
Western Canada and USA	Copernicus GLO-30
Arctic Canada North	ArcticDEM v4.1
Arctic Canada South	ArcticDEM v4.1
Greenland and Greenland Periphery	ArcticDEM v4.1
Iceland	ArcticDEM v4.1
Svalbard	ArcticDEM v4.1
Scandinavia	ArcticDEM v4.1
Russian Arctic	ArcticDEM v4.1
High Mountain Asia	Copernicus GLO-30
Low Latitudes	Copernicus GLO-30
Southern Andes	Copernicus GLO-30
New Zealand	Copernicus GLO-30
Antarctic ice sheet, ice shelves and periphery	REMA v2, filled with Gapless REMA or Copernicus DEM based on local quality.

DEM post-processing

Both ArcticDEM v4.1 and REMA v2 require a post-processing step to be applied to fill missing data gaps. In the case of ArcticDEM, these gaps are small and can be filled effectively with basic linear interpolation.

In REMA v2, data gaps vary in size and complexity, and artefacts are also present in the final DEM. As such, we employ a more complex post-processing approach. In each case, we assess the most suitable filling method and filled gaps and artefacts with either Gapless REMA or Copernicus DEM, depending on a manual expert assessment of local quality. This is preferable to spatial interpolation in these regions as many artefacts are in areas of complex terrain.

4.1.2 Region Masks

For each glacier region, we take the vector mask as defined in v7 of the Randolph Glacier Inventory.

For the Antarctic Ice Sheet, Antarctic Ice Shelves, and Greenland, we use the ice mask as defined by BedMachine (v5 for Greenland (Morlighem M. e., 2022), v3 for Antarctic regions (Morlighem M. , 2022) (Morlighem, et al., 2020)). The raster BedMachine mask is vectorised and only the polygon with the largest area is used in the EOLIS processing. This ensures that the mask encompasses the ice sheets whilst minimising the presence of peripheral RGI glaciers in the final mask.

4.1.3 Uncertainty Calibration Data Set

ATL06 v6 (ATLAS/ICESat-2 L3A Land Ice Height; Advanced Topographic Laser Altimeter System) data (Smith, et al., 2021) is used as a reference data set for all EOLIS regions.

4.1.4 Input Swath Elevation Data

Before the uncertainty score is calculated, the following baseline filters are applied to the swath elevation data to remove any weak signal and poor-quality data:

- Power in Decibels > -180 dB
- Coherence > 0.5
- Absolute difference to a reference DEM < 150 m
- Median absolute deviation of swath compared to reference DEM (compute within a single waveform) < 50 m

These filters are based on standard filter criteria used in the CryoSat+ CryoTop / CryoTop evolution ESA STSE projects (Gourmelen, et al., 2018) and then adapted based on comparisons to the reference dataset (ICESat2 (Smith, et al., 2021)) to find values which minimised the standard deviations of the elevation difference whilst also maintaining an optimal volume of points.

4.1 Point Product Algorithm Description

4.1.1 Swath Processing

The surface elevation is retrieved from CryoSat-2 swath data by resolving ambiguous phase signals, first splitting individual waveforms into separate segments in order to handle signals retrieved from multiple surfaces being measured within a single waveform.

4.1.1.1 Waveform segmentation

It is common for a single waveform to contain multiple correct phase ambiguity solutions, arising where the retrieved signal arrives from multiple directions within a single waveform or when phase unwrapping has been unsuccessful. Solving for multiple phase ambiguities within a single segmented waveform improves geolocation accuracy. This results in increased data volume and product coverage, since the algorithm succeeds in identifying high quality solutions for an increased volume of waveforms. Figure 3 shows an example of such a waveform; a higher quality solution is achieved when the waveform is treated as multiple segments.

Figure 3: Example waveform with segments. Top: Phase difference and coherence against sample number for this waveform. Bottom: elevation against longitude for the phase ambiguity solutions (grey) and the reference DEM (black). The chosen phase ambiguity solution

Waveform indexes where the waveform should be broken into segments may be identified in two distinct ways:

- There may be a jump in the unwrapped phase, indicating that the signal is arriving from a different direction, or where phase unwrapping was unsuccessful

- There may be a continuous series of poorly defined data points (interpreted as NaN values).

Indexes may be treated as the end index of a waveform segment if there is either a large phase jump, or a series of NaN values comes to an end. Here we describe how each of these are identified and used to split the waveform into separate segments.

4.1.1.2 Identifying phase jump segments

Unwrapped phase difference

The phase difference $\Delta\varphi_{unwrapped,i}$ for each index i in the waveform is computed as follows:

$$\Delta\varphi_{unwrapped,i_i} = \varphi_{unwrapped,i+1} - \varphi_{unwrapped,i} \qquad where\ \varphi_{unwrapped} \in R$$

Where $\varphi_{unwrapped,i}$ and $\varphi_{unwrapped,i+1}$ are the unwrapped phases for index i and the subsequent index $i+1$, respectively. Only finite values of phase are considered, with non-finite values removed before the difference is computed. Note that this difference in indexing from removing non-finite values is considered when locating the index where the phase jump occurs.

Identifying segments

Phase jumps in the waveform are identified as follows:

$$|\Delta\varphi_{unwrapped,i}| > \Delta\varphi_{unwrapped,min}, where\ \Delta\varphi_{unwrapped,min} = \frac{1}{2}\pi$$

In algorithm testing we have found that a $\Delta\varphi_{unwrapped,min} = \frac{1}{2}\pi$ is a suitable threshold for this purpose as it is fairly permissive, and allows for small phase jumps to be identified. Multiple phase jumps may be present in a single waveform; as such the output of the phase jump search is a list of indices that define the ends of waveform segments.

4.1.1.3 Identifying NaN sequence segments

Identifying segments

We identify segments of the waveform where the unwrapped phase is undefined as follows. First, a binary mask variable M is defined which denotes whether an index in the waveform has an undefined unwrapped phase:

$$M_i = 0\ if\ \varphi_{unwrapped,i} \neq NaN$$
$$M_i = 1\ if\ \varphi_{unwrapped,i} = NaN$$

Next, the difference between subsequent mask values is evaluated:

$$\Delta M_i = M_{i+1} - M_i$$

This difference variable is used to identify sequences of NaNs; if $\Delta M_i = -1$, then index i denotes the last index in a segment of NaNs and index $i + 1$ defines the start of a new segment (with $\Delta M_{i+1} = 1$). Lists of the indices where the NaN segments begin and end are created:

$$p_{start} = \{i \mid \Delta M_i = 1\}$$
$$p_{end} = \{i \mid \Delta M_i = -1\}$$

If either p_{start} or p_{end} contain no indices, we proceed solely with the segmentation indices identified from phase jumps. Otherwise, cases where the waveform either starts or ends with a NaN value are accounted for as follows. The list of segment end indices is checked, and any individual indices $p_{end,j}$ that occur before the lowest segment starting index are removed. The resulting list of $p_{end,j}$ should all be greater than the lowest segment starting index:

$$p_{end,j} > p_{start,min}$$

Next, if the length of list p_{start} is larger than the length of list p_{end}, then the final starting index is removed:

$$p_{start,j} < p_{start,max}$$

Any NaN sequence segments with a length below a minimum defined number ($N_{NaN,min}$) are discarded. The NaN sequence length N_{NaN} for each segment j is computed as:

$$N_{NaN,j} = p_{end,j} - p_{start,j}$$

We have found that a value of $N_{NaN,min} = 50$ is suitable as it allows for identification of small segments whilst avoiding over-segmentation of the waveform.

$$ind = \{p_{start,j} \mid N_{NaN,j} > N_{NaN,min}\}$$

4.1.1.4 Segmenting the waveform

When the phase jump and NaN sequence start indexes are identified, any duplicate indexes are removed and the resulting indices are used to split the waveform. For example, if two segment end indices have been identified in a waveform at index i and j, then assuming a start index of 1, a waveform of length 1024 would be split into the following three segments:

1. From 1 to i
2. From $i + 1$ to j
3. From $j + 1$ to 1024

If no indexes for waveform segmentation have been located, then the waveform is not segmented.

4.1.1.5 Solving for phase ambiguities

The optimal phase ambiguity solution index is identified separately for each segment using a combined weighted mean solver. The phase ambiguity solver procedure takes as input the phase ambiguity solutions for a given waveform and determines which of these is the best solution for the data. Throughout this section we use the subscript $\boldsymbol{i}$ to denote metrics that are computed across a waveform, and the subscript $\boldsymbol{j}$ to denote metrics that are computed as comparisons between different phase ambiguity solutions. We first define the swath weights per sample number and the different weighted mean solver statistics, and then describe how these are applied to select the best phase ambiguity solution.

4.1.1.6 Weights

Each sample in the waveform is assigned a weight for use in calculating the weighted mean solver statistics. The weight per sample number i is computed as:

$$\omega_i = P_{norm,i} \cdot C_i$$

$$\omega_i = 2 \cdot \omega_i \quad if\ 250 \leq sample\ number_i \leq 1000$$

Where C_i is the signal coherence for sample number i and $P_{norm,i}$ is the signal power in decibel watts, normalised to between 0 and 1 to match the coherence scale. To perform this normalisation a minimum and maximum power are calculated:

$$P_{max} = max([max(P), -140])$$

$$P_{min} = min([min(P), -220])$$

$$P_{norm,i} = \frac{P_i - P_{min}}{P_{max} - P_{min}}$$

Weights are boosted by a factor of 2 if the sample number is between 250 and 1000, to account for artefacts in the leading edge of the waveform due to phase model characteristics.

4.1.1.7 Weighted mean solver statistics

Weighted mean metrics are computed from the swath elevation data for each phase ambiguity in order to select the best overall solution.

Weighted MAE

The weighted mean absolute error ($wMeanAE_j$) of a phase ambiguity solution j is the weighted average of the absolute differences in elevation with respect to the reference DEM:

$$wMeanAE_j = \frac{\sum_i^N \left| h_{i,j} - h_{DEM,i} \right| \times w_i}{\sum_i^N w_i}$$

Where $h_{i,j}$ is the swath elevation for sample number i and phase ambiguity solution j, $h_{DEM,i}$ is the DEM elevation for sample number i, w_i is the weight for sample number i, and N is the total number of samples in the waveform.

Weighted MAD

The weighted mean absolute deviation of a phase ambiguity solution is a measure of the dispersion of the points around the average elevation difference:

$$wMeanAD_j = \frac{\sum_i^N |d_{i,j} - <d>_j| \times w_i}{\sum_i^N w_i}$$

Where $d_{i,j} = h_{i,j} - h_{DEM,i}$ is the difference between the measured swath elevation and the reference DEM, and $< d >_j$ is the weighted average elevation difference:

$$< d >_j = \frac{\sum_i^N (h_{i,j} - h_{DEM,i}) \times w_i}{\sum_i^N w_i}$$

Normalised Weighted Metrics

The normalised weighted mean absolute error and deviation allow direct comparison of the two metrics, since they may span different ranges. The normalised weighted mean absolute error is defined as:

$$wMeanAE_{Normalised,j} = \frac{wMeanAE_j - min(wMeanAE)}{max(wMeanAE) - min(wMeanAE)}$$

Where $wMeanAE_j$ is the weighted mean absolute error for phase ambiguity solution j, and $min(wMeanAE)$ and $max(wMeanAE)$ are the minimum and maximum weighted mean absolute errors across all phase ambiguity solutions, respectively.

Similarly, the normalised weighted mean absolute deviation is defined as:

$$wMeanAD_{Normalised,j} = \frac{wMeanAD_j - min(wMeanAD)}{max(wMeanAD) - min(wMeanAD)}$$

Where $wMeanAD_j$ is the weighted mean absolute deviation for phase ambiguity solution j, and $min(wMeanAD)$ and $max(wMeanAD)$ are the minimum and maximum weighted mean absolute deviations across all phase ambiguity solutions, respectively.
These normalised metrics are added together to give a combined weighted score per phase ambiguity solution j:

$$wScore_j = wMeanAE_{Normalised,j} + wMeanAD_{Normalised,j}$$

4.1.1.8 Application of phase ambiguity solver methods

In this Section we describe how these weighted mean metrics are used to select the best phase ambiguity solution for the weighted mean combined method, and how to handle edge cases.

Weighted mean combined solver
For each phase ambiguity solution, we remove samples where the swath elevation is undefined. Then the weights are computed for each remaining sample in the waveform. Next, the $wMeanAE_j$ and $wMeanAD_j$ are computed for each phase ambiguity solution using the weights and the elevations given by each solution.

If there are < 100 finite elevation difference measurements then the phase ambiguity solution with the minimum $wMeanAE$ is chosen.

The phase ambiguity solution with the lowest combined score $wScore_j$ is selected. If this solution has a $wMeanAE$ >150m, then the chosen solution instead becomes the solution with the lowest $wMeanAE$. This approach minimises both the dispersion in the elevation differences and the absolute error whilst not placing an explicit limit on the absolute error to allow for areas of large change.

Edge cases
Additional criteria are placed on the swath points and solver metrics to catch edge cases with ill-defined solutions:

- If all waveform points have a weight of zero, then no solution is identified.
- If all ambiguity solutions have one or both of $wMeanAE$ and $wMeanAD$ equal to NaN, then no solution is identified.
- If all points have a $wMeanAD$ equal to zero, then the solution with the minimum $wMeanAE$ is chosen. This is to handle edge cases where there are only two data points in the waveform and one has a weight of zero.

4.1.5 Phase Model Adjustment

Due to CryoSat-2's slight mis-pointing, the conversion from interferometric phase to angle of arrival is complex and leads to systematic errors in the angle of arrival (Wingham, Phalippou,

Mavrocordatos, & Wallis, 2004; Recchia, Scagliola, Giudici, & Kuschnerus, 2017). These errors are a function of surface slope, roll angle and distance from POCA. This affects predominantly areas of low surface slopes and leads to artefacts in the EOLIS elevation products (Figure 4).

Ice Sheets

We mitigate this effect using a simple empirical model applied on a waveform basis to the elevation difference between swath and a reference DEM, taking advantage of the systematic nature of the error. For this, the swath waveforms are split into two sections: the *leading edge*, and *non-leading edge*. The *leading-edge* section begins at the POCA and continues until the return signal power peaks. The *non-leading edge* begins at the trailing edge until the end of the swath waveform. A robust linear model is fit to the data within the *leading-edge* section, and a two-part piecewise linear model fit to data within the *non-leading edge*. The model is then applied to the original swath data, ensuring that the mean elevation difference between swath and the reference model is maintained. Underlying topography is considered when applying the adjustment such that only very flat areas with low slope are adjusted. The degree of improvement of the model is also measured to determine if the adjustment should be applied. This approach works well to greatly reduced features present in the product, with only minor residuals remaining (Figure 4).

Ice Shelves

For the Antarctic Ice Shelves, a physics-driven correction is used to mitigate the systematic errors, for this purpose a dedicated phase correction plugin was developed by Aresys (Recchia, Scagliola, Giudici, & Kuschnerus, 2017).

Glaciers

No correction is necessary for the glacier regions, as they typically have higher slopes and more complex topography.

4.1.6 Tide Correction

Tide correction with CATS2008: a tide correction is applied to the Swath processed data, using the Circum-Antarctic Tidal Simulation Model (CATS2008; Padman et al. (2002), Padman et al. (2008)). The CATS2008 tide model is used to calculate tidal heights at a specific point in space and time. The elevation variations observed by the EOLIS point data due to tidal changes are then corrected by subtracting the tidal elevation from the EOLIS point data.

Figure 4: Example of improvement of phase model features in north Greenland. Top: elevation difference between the CryoTEMPO-EOLIS Greenland ice sheet gridded product for February 2019 and the CryoTop Greenland gridded DEM (Gourmelen, et al., 2018) before (left) and after (right) the adjustment is applied. Bottom: elevation difference profile over the red line marked in the spatial plot (top), showing the reduction in amplitude of features after the adjustment is applied.

4.1.7 Point Product Uncertainty Score

For each swath elevation measurement an uncertainty value is calculated using a binning approach with several variables associated with measurement quality. This provides a simple metric on which the data can be filtered to a desired precision. This section outlines the elevation uncertainty algorithm.

Firstly, for each region, the swath data is compared to a reference elevation:

$$\Delta E = E_{swath} - E_{ref}$$

where E_{swath} and E_{ref} are the swath and reference elevations respectively joined within a 10-day time window and 50m radius. As described in Section 4.1.3, the reference dataset used is ICESat-2 ATL06 (v6). A slope correction is applied to ΔE to minimise errors due to variation in topography within the 50m joined distance. The differences, ΔE, are made up of errors in swath dataset, errors in the reference dataset, signal penetration differences between $E_{swath}$and E_{ref}, errors due to variation in elevation within the 10-days period, errors in the slope correction of the 50m joined criteria, as well as other systematic differences. Consequently, it cannot directly be used as a measure of data uncertainty.

A binning approach is then used to calculate median absolute deviations of the elevation differences ΔE using bins of five different variables, known to impact swath uncertainty (Table 2).

Table 2: Swath point data variables used for elevation uncertainty calibration.

Power in Decibels	As defined in the CryoSat-2 Product Handbook (ESA, 2019)
Coherence	As defined in the CryoSat-2 Product Handbook (ESA, 2019)
Along Track Slope	Slope is calculated along the track at a length scale of 400m (the along track resolution stated in ESA CryoSat-2 Product Handbook (ESA, 2019)). Along track slope is defined as change in elevation in metres between 200m in front and 200m behind the observation divided by 400m.
Across Track Slope	Slope is calculated across the track at a length scale of 1600m (the across track pulse limited footprint stated in ESA CryoSat-2 Product Handbook (ESA, 2019)). Across track slope is defined as change in elevation in metres between 800m to the left and 800m to the right of the observation divided by 1600m.
Roughness	Calculated from the reference DEM as the largest difference of a central pixel and its surrounding cells.

A five-dimensional cube consisting of each variable binned into 8 equal volume bins is generated. The data is sampled using every bin combination across all variables resulting in 8^5 (= 32,768) "quality bins". The quality bins are calculated separately for Antarctic Ice Sheet, Antarctic Ice

Shelves, Greenland Ice Sheet and the glacier regions. The Median Absolute Deviation (MAD) of the elevation differences is calculated from the binned sample data:

$$MAD_{\Delta E} = median(|\Delta E - median(\Delta E)|)$$

and is defined as the uncertainty value for each of the quality bin combinations.

The quality bins are then used as a lookup table, where each individual swath elevation measurement is matched to an uncertainty, given its five variable values (see Table 2). It should be noted that the uncertainty metric provided is not a guarantee that the elevation is accurate to within the uncertainty score given; it is a conservative estimate of the uncertainty for a point but does not guarantee the point is not an outlier.

4.1.8 Definition of region groupings for uncertainty calculation

EOLIS regions are grouped into four categories for the purposes of calculating and assigning uncertainties. These groups are defined as follows (in parenthesis the number of each RGI region):

Table 3: Summary of uncertainty region groupings

Region Group Name	EOLIS Region Names
Greenland Ice Sheet	Greenland Ice Sheet
Antarctic Ice Sheet	Antarctic Ice Sheet
Antarctic Ice Shelves	Antarctic Ice Shelves
RGI regions	Alaska (01), Western Canada & USA (02), Arctic Canada North (03) and South (04), Greenland Periphery (05), Iceland (06), Svalbard (07), Scandinavia (08), Russian Arctic (09), Central Europe (11), Central/South West/South East Asia (13, 14, 15), Low Latitudes (16), Southern Andes (17), New Zealand (18) and Antarctic Periphery (19)

4.2 Point Product Uncertainty Score Output

The point product uncertainty algorithm provides a five-dimensional cube consisting of the five variables binned into eight equal volume bins with associated median absolute deviation for each combination (Table 4). For each swath point, the associated variables are matched to the bin definitions and the estimated uncertainty score for that bin is assigned to the swath point.

Table 4: Definition of uncertainty bins for Greenland Ice Sheet, Antarctic Ice Sheet, Antarctic Ice Shelves, and the RGI regions. Each bin is between two bin edges, e.g. 0-1, 1-2 …. 5-6.

Greenland Ice Sheet

Bin Edge	Power [dB]	Coherence	Roughness [m]	Slope Across	Slope Along
0	-180.00	0.500	0.00	-0.6507	-1.3475
1	-163.7963	0.651	0.9062	-0.0160	-0.0121
2	-160.2568	0.751	1.4219	-0.0087	-0.0053
3	-157.3138	0.822	2.0547	-0.0048	-0.0021
4	-154.5933	0.873	2.8438	-0.0023	0.0001
5	-151.8576	0.910	3.8906	0.0010	0.0023
6	-148.9532	0.938	5.5000	0.0049	0.0054
7	-145.2781	0.961	8.7812	0.0122	0.0117
8	0.0000	1.000	515.7656	0.7041	1.1862

Antarctic Ice Sheet

Bin Edge	Power [dB]	Coherence	Roughness [m]	Slope Across	Slope Along
0	-180.0000	0.500	0.00	-0.6613	-1.2862
1	-164.6029	0.636	0.7031	-0.0140	-0.0116
2	-160.9390	0.725	1.1719	-0.0069	-0.0051
3	-157.9959	0.794	1.7188	-0.0035	-0.0021
4	-155.3528	0.848	2.4219	-0.0013	0.0001
5	-152.8438	0.890	3.4219	0.0004	0.0024
6	-150.1981	0.924	5.0078	0.0030	0.0055
7	-146.7744	0.952	8.3047	0.0098	0.0122
8	0.0000	1.010	602.4609	0.6170	2.0680

Antarctic Ice Shelves

Bin Edge	Power [dB]	Coherence	Roughness [m]	Slope Across	Slope Along
0	-180.00	0.500	0.00	-0.2477	-0.4488
1	-163.1773	0.636	0.0625	-0.0010	-0.0012
2	-160.2312	0.696	0.1016	-0.0004	-0.0004
3	-157.5517	0.738	0.1562	-0.0002	-0.0002
4	-154.9748	0.774	0.2266	0.0000	0.0000
5	-152.3753	0.813	0.3438	0.0001	0.0002
6	-149.5555	0.863	0.5625	0.0003	0.0004
7	-146.1250	0.921	1.1406	0.0008	0.0012
8	0.0000	1.000	208.8906	0.1666	0.2121

RGI regions

Bin Edge	Power [dB]	Coherence	Roughness	Slope Across	Slope Along
0	-180.00	0.500	0.00	-3.2720	-15.2512
1	-168.4878	0.603	4.7812	-0.0462	-0.0524
2	-166.1640	0.686	6.9141	-0.0255	-0.0251
3	-163.9142	0.756	9.1250	-0.0124	-0.0109
4	-161.4258	0.817	11.7578	-0.0009	0.0006
5	-158.6067	0.870	15.3594	0.0110	0.0125
6	-155.3472	0.915	21.0547	0.0241	0.0269
7	-151.3089	0.953	33.5469	0.0450	0.0551
8	0.0000	1.000	7293.5791	3.2390	16.7816

4.2.1 Choice of Uncertainty Score Variables

For each variable used in the uncertainty calculation (see Table 4) there is a clear link between the value of the variable and the uncertainty score (Figure 5).

Note that Figure 5 illustrates the relationship between uncertainty and each individual variable as a comparison exercise, however the uncertainty calculation is a combination of all variables and thus is a five-dimensional. Higher slope of the underlying terrain results in a higher uncertainty score: this is observed for *Along Track Slope* and A*cross Track Slope*. Swath data with high power in decibels results in a lower uncertainty score, with the opposite applying for low power data points. Similar linear correlations are observed for coherence where high coherence data has a low uncertainty score and low coherence data has a higher uncertainty score. Finally, we see that data with low roughness, a measure of the irregularity of the surface, has a low associated uncertainty score, and higher roughness results in higher uncertainties.

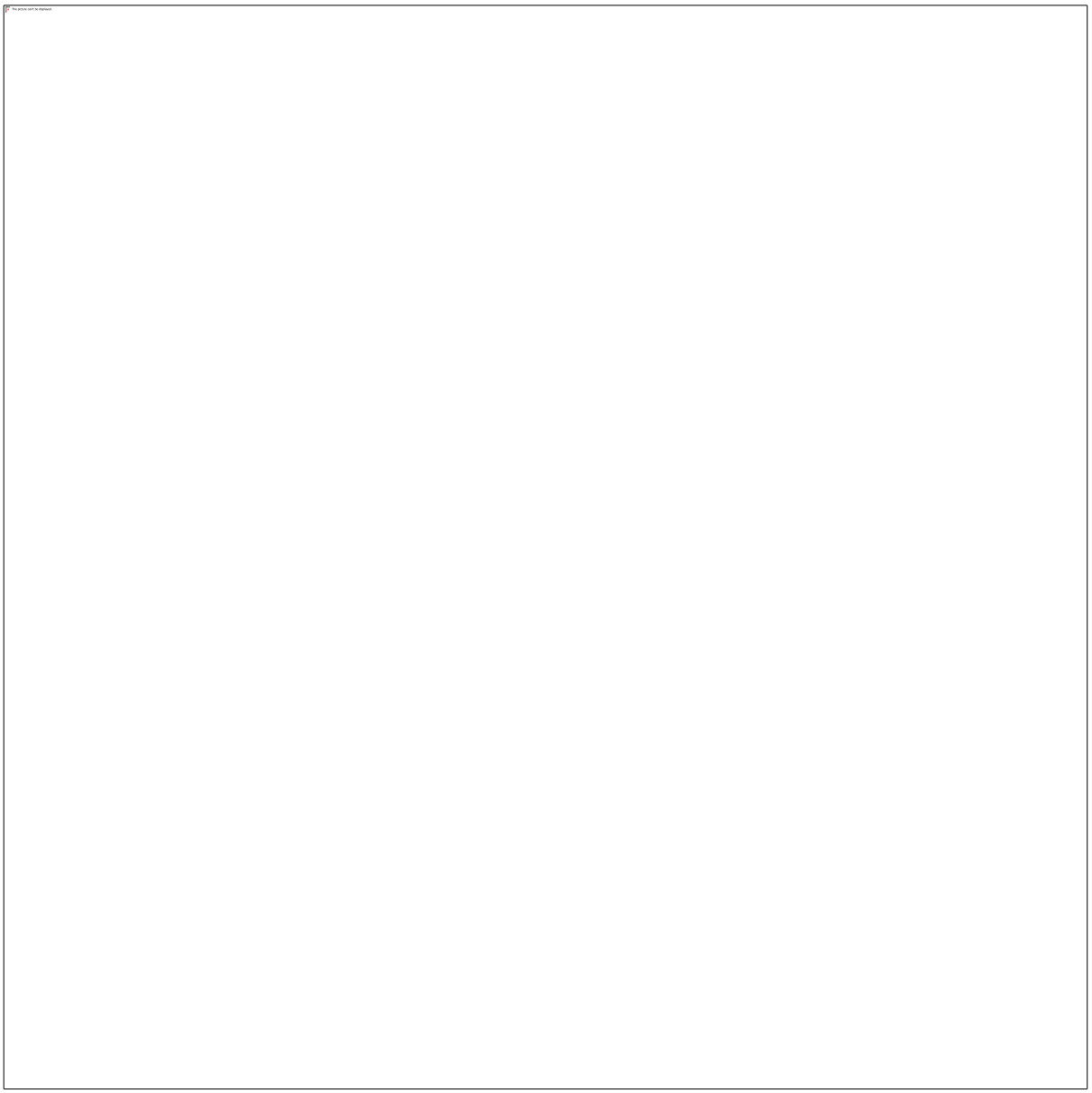

Figure 5: Comparison of uncertainty calculated using equal volume bins of points for each variable for Greenland Ice Sheet (blue), Antarctic Ice Sheet (orange), Antarctic Ice Shelves (green), and the RGI regions (red).

4.2.2 Uncertainty Score Filter

The published EOLIS point product is filtered to only include points below a maximum uncertainty of:

- 20m for all glacier regions
- 7m for the Greenland and Antarctic Ice Sheets, and the Antarctic Ice Shelves.

This uncertainty filter is also applied in the creation of EOLIS gridded products.

5 Gridded Products

5.1 Monthly Gridded Elevation

5.1.1 Scope and Coverage

The CryoTEMPO-EOLIS monthly gridded products are DEMs that provide users with instant access to gridded and averaged point data at 2km spatial resolution. The CryoTEMPO-EOLIS DEMs are a valuable tool to monitor changes in topography at monthly temporal resolution. Monthly gridded products are published for the following regions:

- Greenland Ice Sheet
- Antarctic Ice Sheet
- Alaska
- Arctic Canada North
- Arctic Canada South
- Greenland periphery
- Iceland
- Svalbard
- Russian Arctic
- Southern Andes
- Antarctic periphery

5.1.2 Input Data

The gridded products are generated using the CryoTEMPO-EOLIS point product data, with each monthly DEM using a 3-month overlapping temporal window which is centred on the middle of the publication month. For consistency, the gridded product uses swath data points that have been filtered using the same filter criteria applied for the point product (see Sections 4.1.4 and 4.2.2).

5.1.3 Algorithm Description

The gridding method uses the methods proposed by Jakob et al. (2021) to handle complex topography in the glacier regions.

There are multiple phases in the construction of the gridded product from the point data, which are detailed below:

1) **Topography removal:** topography is removed from the gridding by subtracting the reference DEM from the swath elevation measurements at a point level (hereinafter referred to as *DEM difference*).
2) **Median calculation:** for each 2km posting, all *DEM difference* values within a 2km radius are combined using a median calculation to create a gridded *DEM difference*.
3) **Quality filtering:** retain pixels with:
    a. Contributing point count > 20, to reduce impact of sample size on gridded aggregation
    b. standard deviation of contributing points < 50m, to remove extreme outliers
    c. Number of unique contributing waveforms > 2, to mimimise impact of singular waveform geolocation errors
4) **Reduction of boundary noise and artefacts:** a 3x3 pixel median filter is applied iteratively 5 times to the gridded *DEM difference* values and analysis of residuals is performed to identify and replace outliers with the local median
5) **Topography retrieval:** the gridded *DEM difference* values are converted back to a DEM using the reference DEM.

5.1.4 Uncertainty Score

Uncertainty Propagation and Spatial Auto-Correlation

The point uncertainty is propagated to a gridded uncertainty, taking spatial auto-correlation into account. An uncertainty estimate is provided for each pixel using the following equation:

$$\sigma_p = \sqrt{\sum_{i}^{n} \frac{1}{n^2}\sigma_i^2 + \sum_{i}^{n}\sum_{j(j\neq i)}^{n} \frac{1}{n^2}\rho_{ij}\sigma_i\sigma_j}$$

where:

$\sigma_p =$ Uncertainty of a pixel

$\sigma_i, \sigma_j =$ Uncertainty of individual points

$\rho_{ij} =$ Spatial auto-correlation between 2 points

$n =$ Number of points contributing to a pixel

This equation reduces to the standard error of the mean uncertainty if all points have 0 correlation. Conversely, if all points are 100% correlated, the uncertainty is the mean of the uncertainties, which is a maximum of 20m given the maximum uncertainty of a point is 20m.

A semi-variogram is used to determine the spatial auto-correlation ρ_{ij} based on the separation of the points. This semi-variogram is calculated using the Python SciKit Gstat library.

For each region a sample of 50,000 is used to derive semi-variograms with: a maximum lag of 5km, an even binning function, the *stable model* and the *Cressie estimator*. Using the sill as an estimate for the covariance and the derived semi-variance, the estimated spatial auto-correlation as a function of distance between points is then calculated as:

$$\rho_{dist} = \frac{Sill - SV_{dist}}{Sill}$$

where:

$\rho_{dist} =$ spatial auto-correlation for a given distance and $SV_{dist} =$ Semi-variance for a given distance

A third order polynomial is then fit to the ρ_{dist} values between 0 and 5km to give an equation that can be used to estimate the spatial auto-correlation.

$$\rho(x) = ax^3 + bx^2 + cx + d$$

where x is the distance between observations. The calculated coefficients are provided in Table 5.

Table 5: Spatial auto-correlation coefficients for the gridded product regions.

Region Name	a	b	c	d
Greenland Ice Sheet	-8.3507e-12	1.0253e-7	-0.0004	0.5281
Antarctic Ice Sheet	-1.0644e-11	1.2415e-7	-0.0005	0.5842
Alaska	-9.7758e-12	1.1881e-7	-0.0005	0.6602
Arctic Canada North	-4.4782e-12	6.2634e-8	-0.0003	0.4188
Arctic Canada South	-3.7021e-12	5.0334e-8	-0.0002	0.3158
Greenland Periphery	-4.4962e-12	5.8803e-8	-0.0002	0.3345
Iceland	-7.3912e-12	9.2701e-8	-0.0004	0.5049
Svalbard	-1.7034e-12	2.3937e-8	-0.0001	0.1646
Russian Arctic	-4.7967e-12	6.0611e-8	-0.0002	0.3249
Southern Andes	-8.3868e-12	1.0394e-7	-0.0004	0.6012
Antarctic Periphery	-3.4479e-12	5.0002e-8	-0.0003	0.5254

Figure 6 shows an example of the spatial autocorrelation as a function of distance, for the Vatnajökull ice cap. This figure shows that for the applicable distance of 4000 m, the auto-correlation is small, and has a maximum of 0.49 when the distance is 0 m. This is expected as two independent observations at the same location will not be identical due to other uncertainties within the signal.

Figure 6: Spatial auto-correlation vs distance for the Vatnajökull ice cap.

Using the spatial auto-correlation, $\rho(x)$, the uncertainty formula shown previously means that in general, low pixel uncertainties of order 1-2 m are seen when there is a high volume of widely distributed points contributing to a pixel. Conversely much higher uncertainties are observed when there is a low volume of points or narrowly distributed points.

Pre-Clustering

To improve computing performance the following intermediate step is used to the calculation of the propagated gridded uncertainty. All points within a specified distance (the pre-clustering radius) are pre-clustered and an effective uncertainty is calculated, assuming that they are all 100% spatially correlated. The reduced dataset is then propagated following the correlation model described in the previous section. This is motivated by the fact that points close to each other are indeed highly (>60%) correlated, and allows faster computation while maintaining a high level of accuracy. For the Greenland and Antarctic ice sheets, a pre-clustering radius of 100m is used. For all other gridded regions, a pre-clustering radius of 50m is used.

5.2 Monthly Gridded Elevation Change

In addition to gridded elevations, the monthly gridded products contain two further variables, which both present a measure of elevation change since a reference period or reference surface:

1) Difference to reference DEM (elevation_difference_to_reference_dem):
    a. This variable is calculated by subtracting the reference DEM for each region from the gridded elevation values derived each month. The resulting grid describes the deviations of the surface measured each month from the reference surface that the DEM provides.
2) Elevation change since reference time (elevation_change):
    a. This variable is calculated using a mean DEM generated from EOLIS data, that describes the average elevations of a region at the start of the CryoSat-2 observing period ($T_0 \approx 2011$). This mean DEM is subtracted from the gridded elevation values each month, resulting in a grid that describes the deviation of the surface measured each month from the surface as it was in 2011.

5.2.1 Difference to reference DEM

Given a reference DEM $E_{x,y}$ and the CryoTEMPO EOLIS gridded product for a specific month $e_{t,x,y}$, the difference to the reference DEM for that month is calculated as:

$$h_{t,x,y} = e_{t,x,y} - E_{x,y}$$

where t is the temporal index and x and y are the spatial indices of a given pixel in projected coordinates.

The reference DEMs used for each region are described in Section 4.1.1. The methods used to generate each DEM vary, as do the contributing data and the time period it covers. As such, the 'elevation_difference_to_reference_dem' variable should be used with caution, with awareness of the differences that may arise if trying to compare directly between regions that use different reference DEMs (in this use case it would be more robust to use the 'elevation_change' variable).

5.2.2 Elevation change since reference time

5.2.2.1 Mean DEM calculation

To calculate a mean DEM, we use as input the EOLIS gridded elevation changes from 2011, spanning January – December inclusive (the first full year of the CryoSat-2 mission), and apply the following processing steps:

1) Per 2km pixel p, we find the mean value of the topography-removed elevation difference grids h_t (see Section 5.1.2) across the 12 months t of data.
    - During the mean calculation, the mean for each pixel $m_{x,y}$ is inversely weighted by the square of the corresponding uncertainty, σ^2 (or the 'variance'), such that more uncertain measurements have a reduced impact on the mean DEM:

$$m_{x,y} = \frac{\sum_t w_t h_t}{\sum_t w_t}, \text{ where: } w_t = \frac{1}{\sigma_t^2}$$

2) We then apply the same median filter used previously to clean the gridded data (point 3 of Section 5.1.2), in order to remove artefacts that might be introduced by averaging across the full year of data.
3) We then fill any missing pixels. This step is necessary to ensure maximum possible coverage in the resulting elevation change grids. If the gridded data is missing any coverage, the coverage will also be missing in all monthly elevation change grids that are subsequently calculated.
    - To fill gaps, we use a Gaussian 2D convolution kernel, to predict missing values $m_{x,y,gap\ filled}$ by smoothing nearby features into large-scale changes:

$$m_{gap\ filled,x,y} = \sum_i w_{G,i} m_{p,i}$$

Where $w_{G,i}$ are the Gaussian kernel weights from within the kernel pixels i. In this process we use a kernel size of 81 pixels (a standard deviation width of 10km), which was found to provide a balance between the inclusion of real variability in the predicted values, whilst avoiding the over-influence of individual noisy pixels in the interpolated grid.

4) We then add the reference topography onto the gridded data to convert to a mean DEM:

$$meanDEM_{x,y} = m_{x,y} + E_{x,y}$$

5) The uncertainty for each pixel in the mean DEM, $\sigma_{meanDEM}$, is calculated by applying the above processing steps to the gridded uncertainty values associated with each gridded elevation measurement. In summary:
    - The uncertainty on the weighted average in each pixel is calculated as:

$$\sigma_{meanDEM,x,y} = \sqrt{\frac{1}{\sum_t w_t}}$$

    - Where gaps in the mean DEM have been filled, we propagate the uncertainties through the Gaussian 2D convolution. In the absence of full spatial autocorrelation analysis, we instead conservatively assume pixels are fully spatially correlated. The propagated uncertainty is calculated as:

$$\sigma_{gap\ filled,x,y} = \sum_i w_{G,i}\ \sigma_{meanDEM,x,y,i}$$

The uncertainties of gap-filled pixels are scaled using fraction $f_{coverage,x,y}$ of pixels within the Gaussian kernel with valid coverage, such that pixels with a low coverage fraction receive a boost in uncertainty:

$$\sigma_{scaled,x,y} = \sigma_{gap\ filled,x,y} \times \sqrt{\frac{1}{f_{coverage,x,y}}}$$

This reflects that the values of gap-filled pixels in areas of low coverage are derived from comparatively little data.

5.2.2.2 Calculation of Elevation Change and associated uncertainty

A mean EOLIS DEM is calculated for each region once per Baseline. It is then subsequently used each month to convert gridded elevations to gridded elevation change. This is simply calculated by subtracting the mean DEM for the region from the monthly gridded topography-removed elevations:

$$\Delta E_{t,x,y} = e_{t,x,y} - meanDEM_{x,y}$$

where t is the temporal index and x and y are the spatial indices of a given pixel in projected coordinates.

The corresponding uncertainty in elevation change is calculated by combining the gridded elevation uncertainties with the uncertainty per mean DEM pixel in quadrature:

$$\sigma_{\Delta E} = \sqrt{{\sigma_e}^2 + {\sigma_{meanDEM}}^2}$$

5.3 Seamless Annual DEMs

5.3.1 Scope and Coverage

The seamless gridded product is a new addition to the suite of CryoTEMPO-EOLIS products. It is an annual Digital Elevation Model (DEM) produced at a spatial resolution of 500m. It combines Swath-processed data from CryoTEMPO-EOLIS, which covers the CryoSat-2 SARIn zone of the ice sheets, with POCA-processed CryoTEMPO Land Ice data (CryoTEMPO, 2025), which additionally provides data over the CryoSat-2 LRM zone. The combination of these datasets allows us to publish the first operational, time-dependent ice-sheet wide gridded dataset produced using CryoSat-2 data. Additionally, Swath-processed gridded data over ice shelves is included in the Antarctic Seamless product.

5.3.2 Input Data

The ice sheet wide gridded product uses two distinct input datasets: (1) the CryoTEMPO-EOLIS point product and (2) the CryoTEMPO Land Ice thematic product.

Swath processing is performed when the CryoSat-2 satellite is in SARIn processing mode. Therefore, for the Antarctic ice sheet and the Greenland ice sheet, the CryoTEMPO-EOLIS point product only covers the ice sheet perimeter and the ice shelves, and not the ice sheet interior (see Figure 7).

The CryoTEMPO Land Ice (CLI) thematic product, which is produced each month for the Greenland and Antarctic ice sheets, covers both the LRM and SARIn mode masks (CryoTEMPO, 2023). It is therefore used as input to the seamless product to fill in missing coverage in the LRM zone.

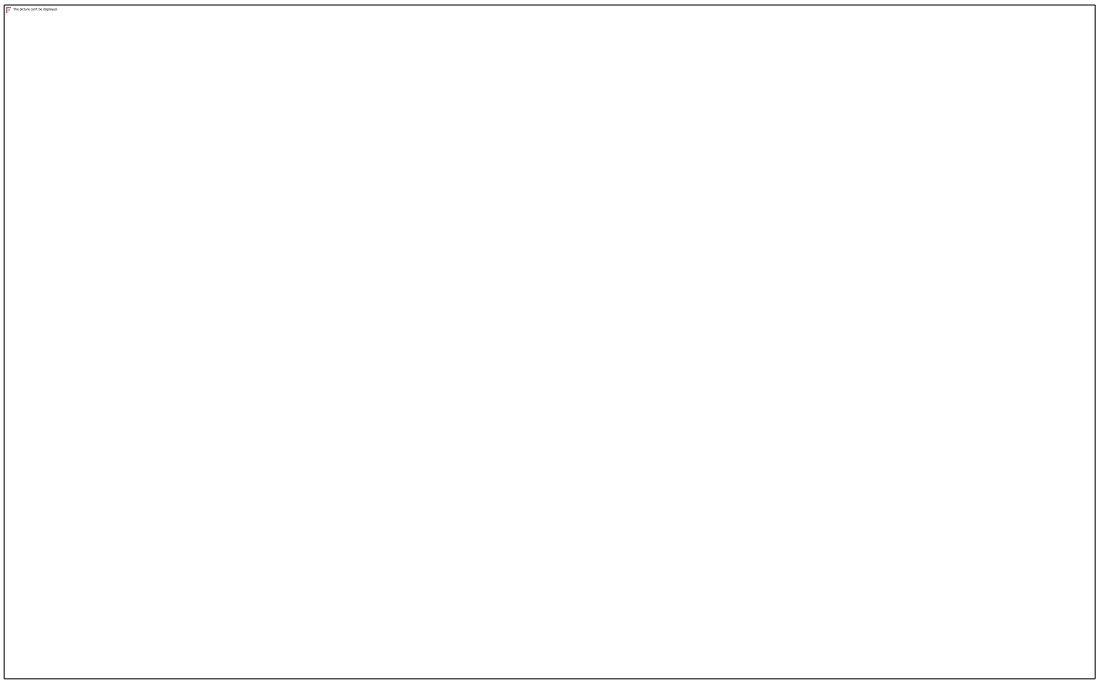

Figure 7: Coverage of the SARIn and LRM zones for the Greenland (left) and Antarctic (right) ice sheets & ice shelves.

5.3.2.1 Velocity Data Sets

We use the MEaSUREs Annual Ice Velocity datasets for both Greenland and Antarctica (Mouginot et al. 2017b) to interpolate missing data in the EOLIS annual DEM. The temporal coverage of the Greenland dataset (https://nsidc.org/data/nsidc-0725/versions/5) is 2014 - 2022, and the temporal coverage of the Antarctica dataset (https://nsidc.org/data/nsidc-0720/versions/1) is 2000 – 2019. When processing each year of data, we use the closest available velocity measurements. If not already supplied as velocity magnitudes, the magnitude is calculated from the individual x and y vector data. In combination with the reference DEM, the velocity dataset is later referred to as the External Drift dataset.

5.3.2.2 Mask Data set

The BedMachine surface type masks are also used for the generation of the seamless products, and are processed to minimise peripheral glacier overlap using the same methods as described in Section 4.1.2. Additionally, we make use of multiple surface type classifications in the processing chain. For Greenland, all 'grounded_ice' is processed as land ice, whilst all 'non_ice_land' is removed from the final product (set to No Data). In Antarctica, 'grounded_ice' and 'lake_vostok' are combined and processed as land ice, and 'floating_ice' is processed as floating ice. Again, all 'non_ice_land' is removed from the final product.

5.3.3 Algorithm Description – Data Preparation

The Swath and CLI datasets described above are gridded separately. The gridding algorithm differs from the algorithm used to generate the monthly EOLIS gridded product. The seamless products are generated at 500m spatial resolution, and at annual temporal resolution. Radial Basis Function gridding is used to grid the input point data. This is described in detail in Section 5.3.3.1. Both annual DEMs are centred on the middle of the publication year i.e. 1st July, and are generated using data from 1st Jan – 31st Dec of each year. The CryoTEMPO-EOLIS input point data is filtered using the same thresholds as described in Sections 4.1.4 and Point Product Uncertainty Score Output4.2.2 for the monthly point data. The CryoTEMPO Land Ice input point data is only filtered using the Swath threshold on the absolute difference to the reference DEM.

5.3.3.1 Radial Basis Function Gridding

To calculate the annual DEM, we need to take into account the temporal and spatial distribution of the data points in each pixel to get a coherent estimate for pixels centred on a specific point in time and space. We utilise a radial basis function (RBF) interpolation method to allow us to weight the points based on their distance to each pixel centre in space and time.

An RBF is a real-valued function, φ, whose value is solely a function of distance from some fixed point, $c = (x_c, y_c, t_c)$.

We use a gaussian RBF: $\varphi(r) = e^{-(\varepsilon r)^2}$; where ε is the shaping parameter, and r is the radius defined as $r = \|c(x, y, t) - p(x, y, t)\|$.

To enable a 3D Euclidean distance calculation for points in space and time we scale the time dimension so that it can be expressed in terms of metres.

$$r(c,p) = \sqrt{\left(x_c - x_p\right)^2 + \left(y_c - y_p\right)^2 + (\lambda t_c - \lambda t_p)^2}$$

Where λ is a scale factor in units of metres per day (as x and y are measured in metres and we define t in terms of days). We define this factor as $\lambda = \frac{spatial\ resolution}{temporal\ resolution}$, so for an annual DEM at 500-meter resolution $\lambda = \frac{500}{365} \approx 1.37$.

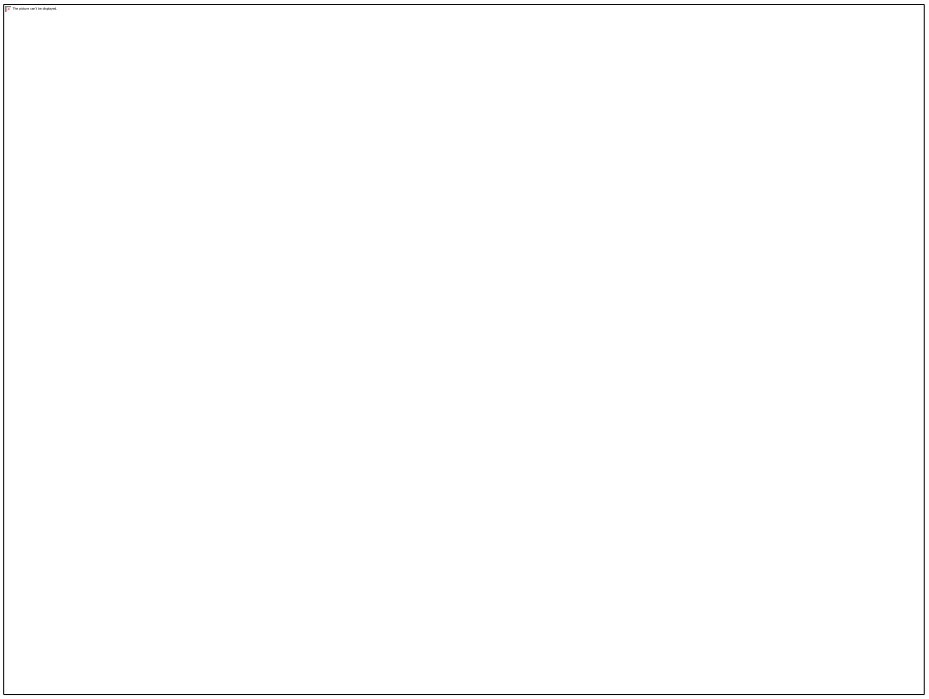

Figure 8: Gaussian radial basis function with our chosen epsilon value of 0.007.

We choose our shaping parameter such that the RBF is approaching 0 at the edge of each pixel. To find this value we can solve the gaussian RBF for where $\varphi(r)$ has decayed by 95 percent: $\varphi(r)$=0.05, and r is set to be equal to half of our chosen resolution.

$$\varphi(r) = e^{-(\varepsilon r)^2}$$

$$0.05 = e^{-(250\varepsilon)^2}$$

$$ln\,(0.05) = -(250\varepsilon)^2 ln\, e$$

$$\varepsilon = \frac{\sqrt{ln\,(20)}}{250}$$

$$\varepsilon \cong 0.007\ \text{m}^{-1}$$

The interpolated value, $f(c)$, from input data values, d, measured at locations p, is a linear combination of the gaussian RBFs centred at p, plus a polynomial, $S(c)$, of degree 0.

$$f(c) = K(c,p)a + S(c)b$$

Where $K(c,p)$ is a matrix of the evaluated gaussian RBFs at each position p. The coefficients a and b are solved by:

$$(K(p,p) + \beta I)a + S(p)b = d \text{ ; noting that } S(p)^T a = 0$$

Where β is a non-negative smoothing parameter that controls how exact we fit the input data. This is currently set at 15. I is the identity matrix.

To manage workload, we limit the number of points used to calculate the interpolant. This limit is currently set to the 200 nearest neighbours. These neighbours are selected from a sub-sample of points that lie within 3 median absolute deviations of the median. The final set is then chosen as the 200 points with the smallest distance according to the distance function $r(c,p)$.

5.3.3.2 Outlier Removal

The next step in the algorithm is to remove outliers from both the CLI and Swath gridded datasets. This is done consecutively for the two datasets, as different configuration parameters are required for each. The outlier removal algorithm aims to identify spatial-temporal outliers, by using the entire temporal seamless annual DEM dataset that is available at the time of processing. At the time of writing, this covers 2011 – 2025, inclusive. Outlier removal is performed per pixel, in each case assessing the how similar the elevation difference of a pixel is to its nearest neighbours, in both space and time. A summary of the outlier removal logical flow is shown in Figure 9.

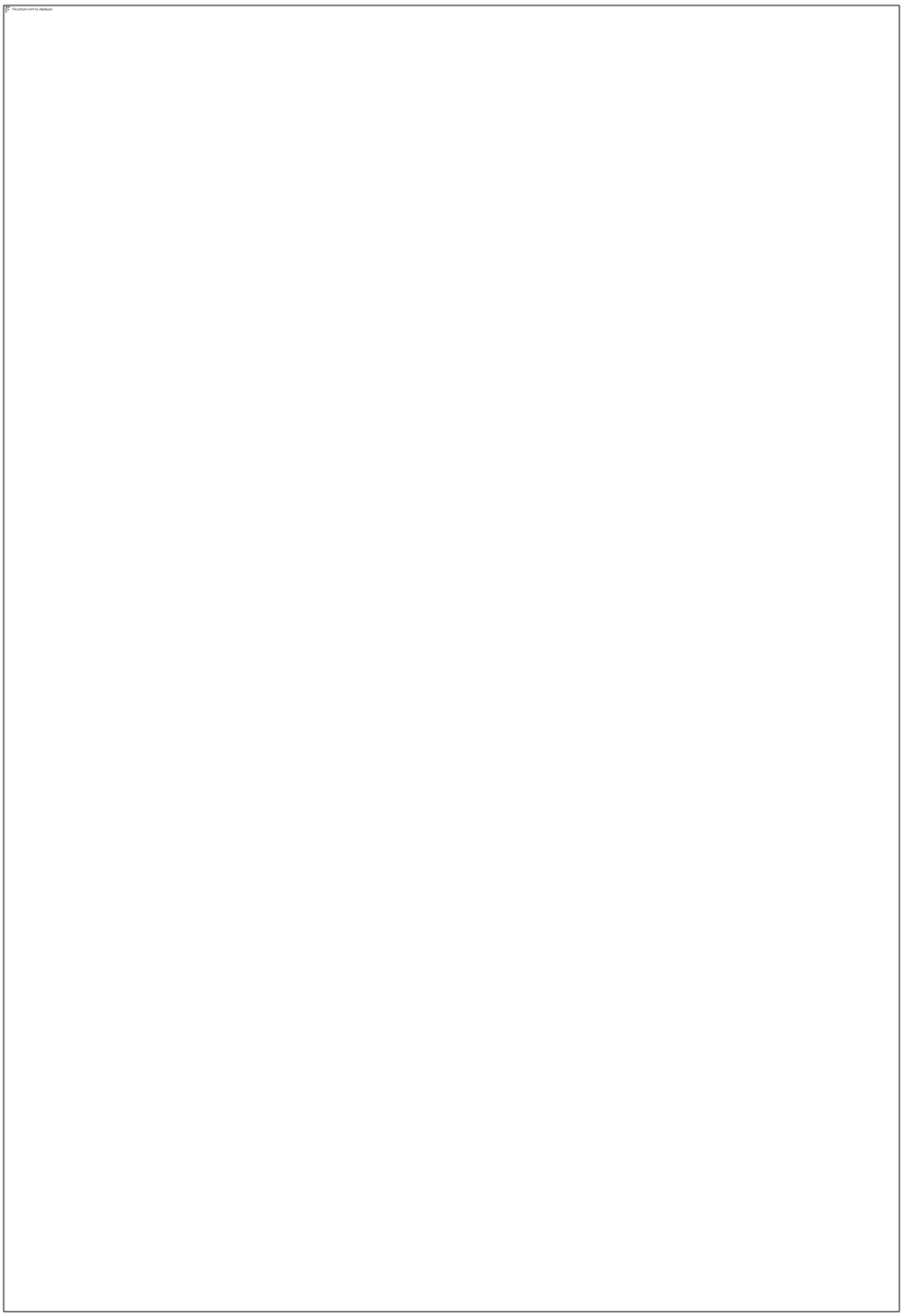

Figure 9: Logical flow of the spatial-temporal outlier removal algorithm

Optimisation using point count and ICESat-2 reference data

To optimise the algorithm, we use other data in combination with the elevation differences of each pixel to assess if the outlier removal algorithm should be run in each case. If we establish that a pixel measurement has a statistically high likelihood of being a valid data point, then we can retain the measurement and avoid running the outlier removal algorithm. To do this, we establish a threshold

of ‘point count per pixel’ above which the outlier removal algorithm does not need to be run. We make use of an external validation dataset to calibrate this threshold. Using the RBF algorithm detailed above, we generate a gridded annual dataset using ICESat-2 ATL06 v6 point data as input. This gives us a gridded validation dataset that can be directly compared to both the Swath and CLI gridded datasets, and assess the accuracy of the elevation difference datasets that they contain.

To perform this comparison, we first calculate differences between coincident Swath / CLI data and ICESat-2. We then bin this dataset using the point count per pixel information, and assess variance of differences with respect to increasing point count per pixel in each bin, to identify threshold above which we should have high confidence in the measurements. This is established to be 2000 contributing points per pixel for Swath data, and 20 contributing points per pixel for CLI data, based on the minimisation of both the median and standard deviation differences above this value, considering consistency across all years of validation data that we used (2019 – 2022 inclusive).

Conversely, using the above investigation we can also infer that if a Swath pixel has fewer than 100 points measurement contributing to its value, we should immediately remove it as an outlier. The consistently high values of differences to ICESat-2 at this value in both plots shown in Figure 10 support this. If a CLI pixel has only one point that contributes to its value, we remove it as an outlier.

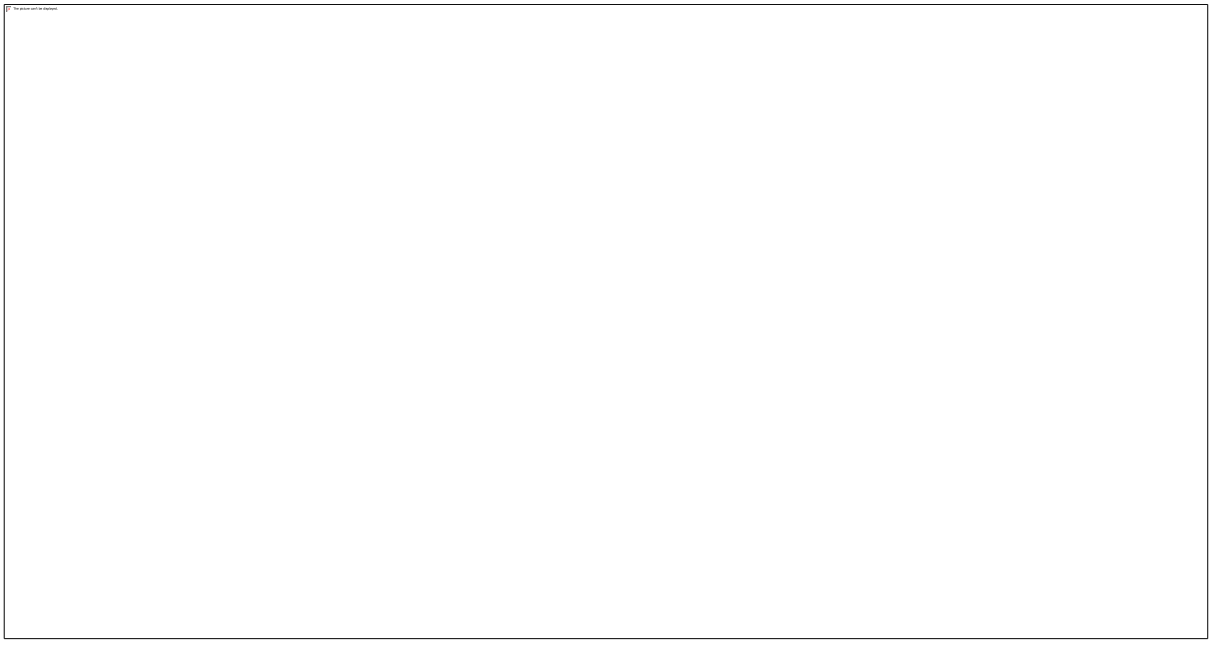

Figure 10: Relationship between point count per pixel and median / std of differences to ICESat-2 for coincident pixels. Generated using Swath data covering 2019 – 2022

Next, the outlier removal algorithm is run per pixel if the contributing point count per pixel is larger than the lower threshold, and less than the upper threshold for the dataset. The following list gives a high-level overview of the processing steps of the outlier removal algorithm:

1. Get nearest neighbour dataset through time, and calculate median elevation change timeseries.

   i. We use a 40 x 40 pixel kernel (20km x 20km) to isolate local area pixels in each case, for each year of data. We then identify the 200 closest neighbours to the pixel that is being checked, and again do this for each year.
2. Gap-fill this timeseries using np.interp1d median fill.
3. If temporal coverage of timeseries > 50% before gap-filling, remove the long-term trend from the dataset using a LOWESS (Locally Weighted Scatterplot Smoothing) filter:
   i. This criteria is used because seasonal decomposition requires a gapless dataset. If original coverage is < 50%, we would be heavily relying on the median fill data within the timeseries to inform the trend removal.
   ii. If coverage is <50%, we don't remove the trend, instead running the remainder of the algorithm on the uncorrected timeseries
   iii. The LOWESS filter is chosen as it can handle extrapolation at either end of the timeseries. This is necessary to ensure that the trend fit is accurate for the final year of data. The number of timesteps considered when fitting each point is set to 50% of the total data points in the timeseries.
   iv. Subtract the fitted long-term trend value from each pixel in the original nearest neighbour timeseries dataset, and recalculate the median and MAD timeseries post-trend removal
4. Compute a moving average of the [median ± 6 x MAD] timeseries, using a 2-year moving window either side of the processing date.
   i. Check if the pixel has a value within the moving average bounds – if it does, we retain this measurement. If it does not, it is removed as an outlier.

Figure 11: An example of outlier identification for a single pixel. Left: gridded data in the local area of the pixel, right: timeseries of measurements of this pixel (purple / green), as well as overall measured change for the local area (pink / black). The outlier in 2019 would be removed in this case.

5.3.3.3 Generation of an Elevation difference map

We generate a map of differences in elevation between the Swath and CLI gridded datasets after outliers have been removed. The difference map is generated at 500m resolution and then various

post-processing steps are performed to generate a map that describes the variation on a larger scale. The following steps are performed:

1. **Subtraction of datasets**: produce a grid of elevation differences (ΔE):

$$\Delta E = E_{CLI} - E_{EOLIS}$$

E_{CLI} = CryoTEMPO Land Ice gridded elevation, E_{EOLIS} = EOLIS gridded elevation

2. **Quality filtering:** remove outliers from the grid of elevation differences. Retain data that satisfies:

$$Q_{25} - 1.5(IQR) < \Delta E_i < Q_{75} + 1.5(IQR)$$

ΔE_i = elevation difference, $IQR = interquartile\ range\ (Q_{75} - Q_{25})$

3. **Smoothing:** a Gaussian 2D convolution kernel is used to smooth the difference map and remove local features.

5.3.3.4 Adjusting and combining the gridded datasets

The ice sheet wide DEM is created by combining CryoTEMPO-EOLIS gridded data covering the SARIn zone with CLI gridded data covering the LRM zone. In this way, we can produce a product that covers the full extent of the ice sheet. The gridded elevations of each dataset are systematically offset vertically, due to the fundamental differences between POCA and swath processing. Therefore, to avoid a discontinuity in elevation at the boundary between the two zones, we adjust the EOLIS gridded elevation values vertically before combining the datasets.

The elevation difference map described in the previous Section is used to adjust the EOLIS gridded elevations in the SARIn zone. For each pixel, the difference map value is added to the EOLIS gridded elevation to produce a grid of adjusted data in the SARIn zone. The grid of adjusted EOLIS data in the SARIn zone is then combined with gridded CLI data in the LRM zone.

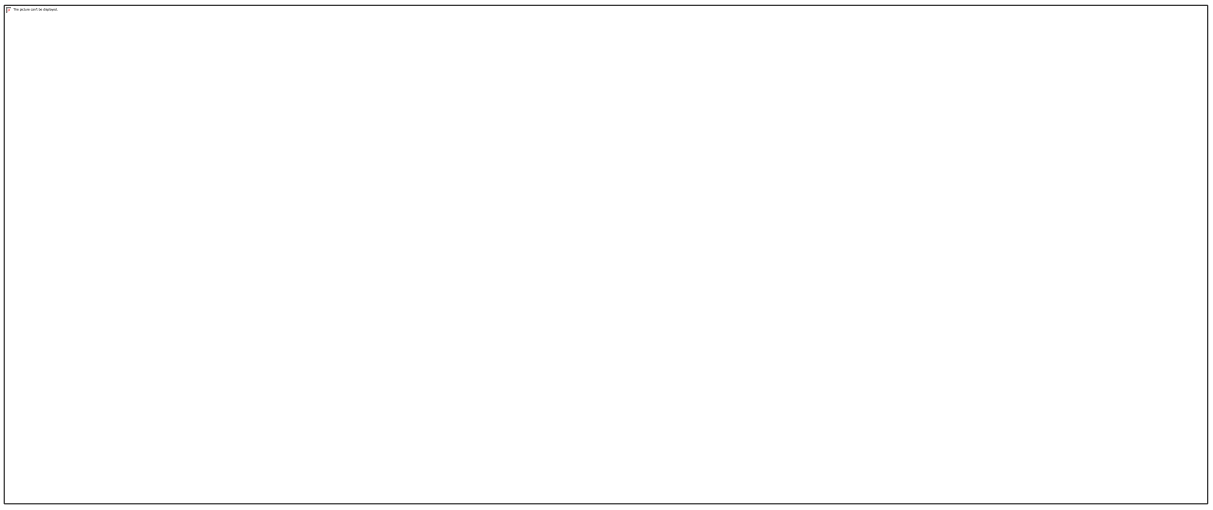

Figure 12: Summary of the processing chain for combining the EOLIS and CLI gridded datasets.

5.3.4 Algorithm Description - Interpolation

There are significant data gaps in the annual DEM that is produced using the algorithms described in Section 5.3.3; both in the LRM zone and in the margins of the ice sheet, especially in regions characterised by complex topography that is hard to observe (see Figure 13). Addressing the absence of data in the margins presents a significant challenge for interpolation, particularly because this is where the most pronounced glacier dynamics occur. To mitigate this issue, we employ two methods of interpolation. The first, External Drift Kriging (EDK), leverages comprehensive external datasets containing variables correlated with our elevation change measurements. This approach aids in refining our interpolation in areas with limited coverage that are undergoing dynamic changes. The second is a linear RBF interpolation technique, this follows a similar approach to that described in Section 5.3.3.1. However, this method defines the RBF as $\varphi(r) = -r$, indicating that the influence of points diminishes linearly with distance. Linear RBF is employed in areas with less complex topography, and smaller continuous areas of missing data e.g. in the LRM zone.

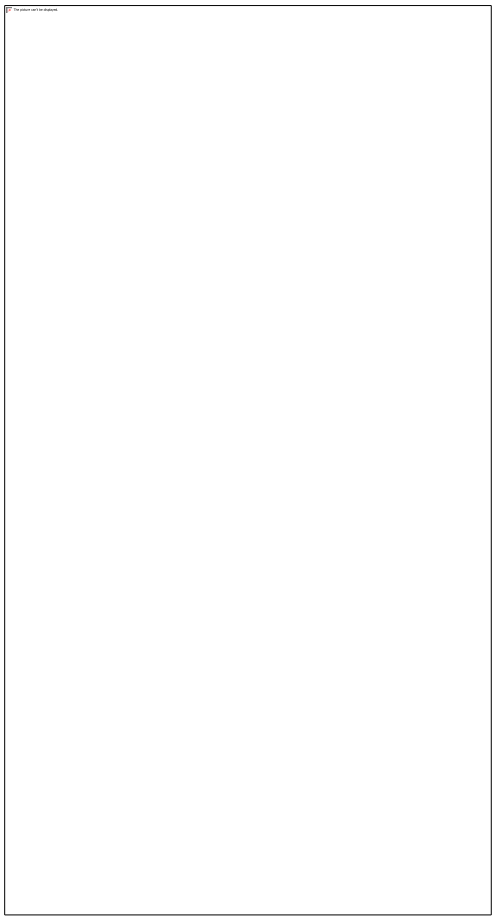

Figure 13: Elevation difference map of 2011 EOLIS annual DEM after gridding, adjusting and combining has been performed. Missing data is highlighted in black.

5.3.4.1 Downsampling

EDK interpolation is computationally intensive, particularly when considering the data volume of the Antarctic Ice Sheet. In order to optimise the processing, and ensure reasonable run times for an operational product, we employed data downsampling to reduce the volume of input points to the Kriging model.

We choose to use an anisotropic downsampling technique, that is informed by the input External Drift dataset. Anisotropic sampling works by calculating the magnitude of the spatial gradient of the input elevation difference dataset. These gradients are then normalised and probabilities per point are calculated by dividing the normalised gradients by the total sum of all gradients. The points are then sampled using these probabilities, meaning that points with higher gradients have a larger probability of being chosen. We modify this approach to calculate the probability of each point (P_i) using the External Drift dataset for additional context:

$$P_i = \frac{NORM(velocity_i) + NORM(\frac{1}{DEM_i})}{\sum_i \left(NORM(velocity_i) + NORM(\frac{1}{DEM_i})\right)}$$

This is done to further increase the sampling rate in areas of high velocity or low elevation.

5.3.4.2 Choice of interpolation method for each data gap

As downsampling is required for EDK interpolation to run in a reasonable time frame, there are significant discontinuities in regions where coverage is sparse but consistent. Therefore, a simpler interpolation method is used in these areas as it provides a more continuous model. EDK will be reserved for dynamic areas in the margins where there are areas of no data. To identify where each interpolation method should be used, we consider the data volume, magnitude of velocities and the regularity with which data is missing across sub areas within a region.

We create a binary mask identifying pixels to be used for External Drift Kriging interpolation. Chosen pixels must have the following properties:

- they are in areas with particularly low coverage
- they are in an area with high surface velocity (above the 80th percentile) and/or they are in an area of low elevations (below the 20th percentile)
- they are not in the LRM zone

The ice sheet is split into 10x10km areas, and the local density of points within each area is considered. The output of this process is a binary mask, which is used as input for the kriging interpolation process. An example of the pixels identified for kriging interpolation vs linear interpolation is shown in Figure 14.

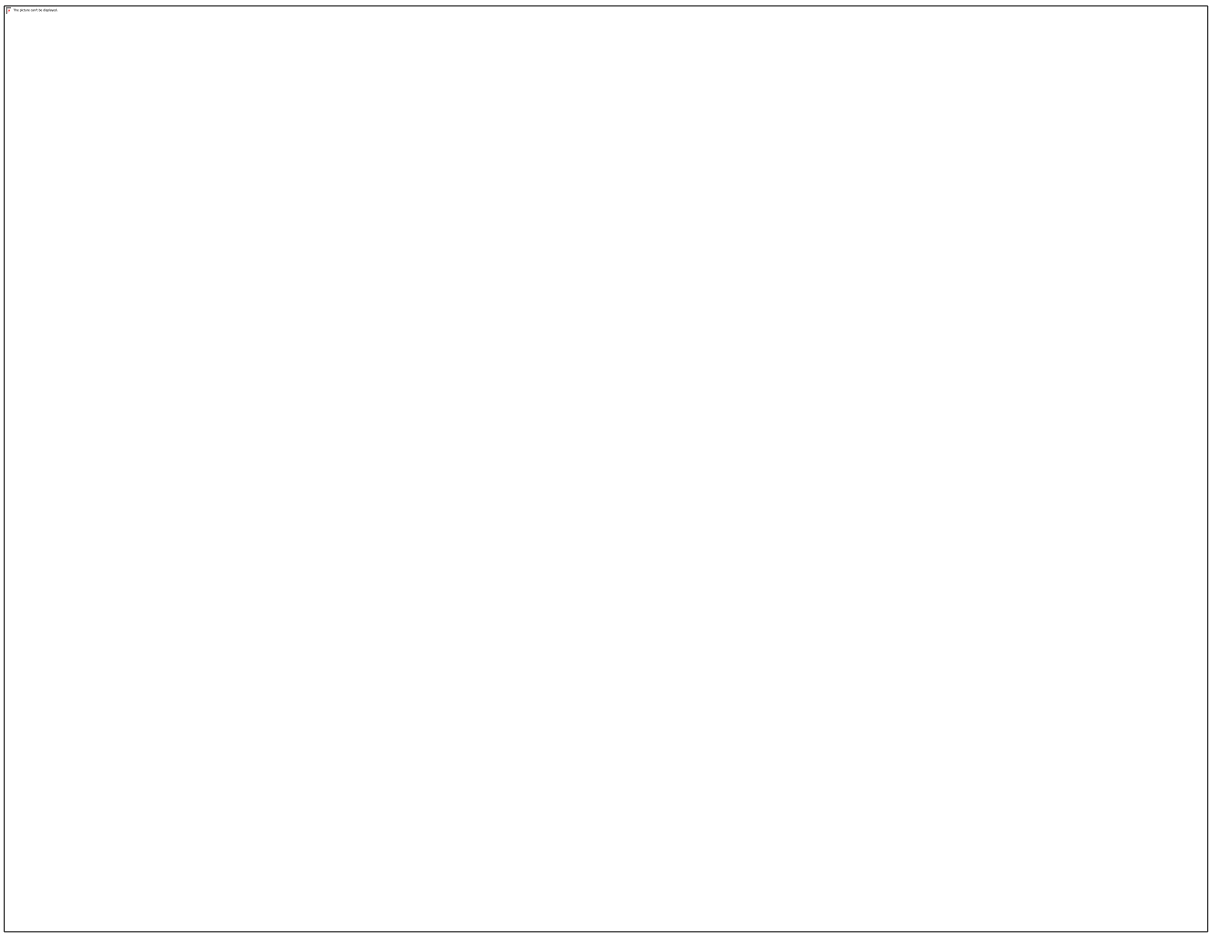

Figure 14: Pixels identified for a) external drift kriging interpolation, and b) basic linear interpolation, in Greenland. SARIn and LRM zones are also shown.

5.3.4.3 External Drift Kriging

Kriging can be understood as a two-step process: first, the spatial covariance structure of the sampled points is determined by fitting a variogram; and second, weights derived from this covariance structure are used to interpolate values for unsampled points or blocks across the spatial field.

An exponential covariance model is used as it was found to minimise the difference between the interpolated and observed values by way of cross-validation.

$$\gamma(r) = \sigma^2 \left(1 - exp\ exp\ \left(-\frac{r}{l}\right)\right) + n$$

Where σ^2 is the model variance, l is the range of the model (the distance at which the maximum semi-variance is reached), and n is the nugget.

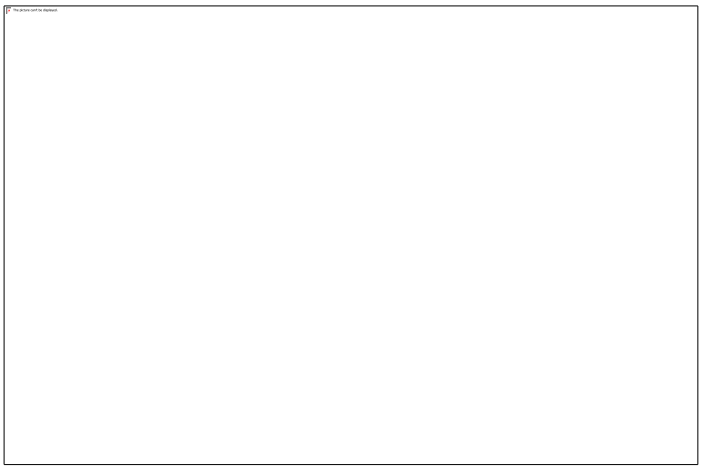

Figure 15: Diagram of an exponential variogram from Interpolation Techniques for Climate Variables, A.D Hartkamp et al. 1999.

In practice, longer length scales and low variance are observed in areas of less complex topography where ice thickness is relatively stable. Closer to the ice sheet margins where roughness and thinning increase length scales decrease and variance increases. However, in areas where coverage is low an ill conditioned fit of the variogram can occur. For this reason, we choose to use one variogram for the full ice sheet. The variogram parameters are defined by choosing 100 random tiles across the entire ice sheet – the same size as used for the interpolation (200x200km with 100km buffer) – and fitting the exponential covariance model to each tile and then calculating the median range, variance and nugget of all models. For both ice sheets, variance = 20, nugget = 5 and median_range = 25km are used when performing the interpolation.

We use external drift kriging to increase the precision of our interpolation using external variables that are correlated with ice thinning, and densely sampled over the full domain, to shape the interpolation:

1. Elevation: At lower elevations with warmer atmospheric conditions and ocean interactions, ice loss is increased compared to high elevations with cooler temperatures where accumulation can occur (Smith et. al., 2020; Box et. al., 2022).
2. Ice velocity: Elevation alone does not capture dynamic thinning. Dynamic thinning of ice occurs in areas of accelerated flow. Warming oceans can significantly increase ice loss through increased ice velocity in marine-terminating glaciers (Smith et. al., 2020; Pritchard et. al., 2023).

In kriging with external drift, the interpolated value at a location s_0 is given by:

$$\hat{z}_{KED} = \sum_{i=1}^{n} \omega_i^{KED}(s_0) \cdot z(s_i)\,;$$

$$\sum_{i=1}^{n} \omega_i^{KED}(s_0) \cdot q_k(s_i) = q_k(s_0)$$

Where z is the target variable (elevation difference) and q_k are the external drift values (velocity and elevation). The weights are solved by:

$$\lambda_0^{KED} = \{\omega_1^{KED}(s_0), \dots, \omega_n^{KED}(s_0), \varphi_0(s_0), \dots, \varphi_p(s_0)\}^T$$
$$= C^{KED-1} \cdot c_0^{KED}$$

Where λ_0^{KED} is a vector of weights, φ is the Lagrange multiplier, C^{KED} is the covariance matrix between points extended with the external drift values at each location, c_0^{KED} is a vector of the extended covariance matrix for s_0.

The kriging variance can be calculated by:

$$\sigma_{KED}^2 = (C_0 + C_1) - c_0^{KEDT} \cdot \lambda_0^{KED}$$

Where the first term is the covariance at zero distance: $C(0) = C_0 + C_1$. Further mathematical definitions of kriging with external drift are provided in Hengl et. al. (2003).

To manage resources the interpolation calculation is split into batches of tiles of 200x200km. Points supplied for kriging are drawn from an additional 100km from the edge of the tile to reduce features at tile edges.

5.3.4.4 Interpolation of Antarctic Ice Shelves

The coverage of the seamless annual DEMs across the Antarctic Ice Shelves is generally high. However, some gaps exist and must be filled by interpolation, similar to the process applied to the ice sheet. Although the general interpolation process is the same for both surfaces, the ice sheet and ice shelf undergo distinct physical processes due to their differing nature.

The Antarctic ice sheet rests on bedrock and experiences thickening and deformation primarily due to accumulation and ice dynamics. In contrast, the ice shelf is a floating extension of the ice sheet, and its dynamics are influenced by oceanic conditions and melting at the ice-ocean interface. These differences result in varied elevation changes across the two surfaces.

Recognising the physical boundary and the distinct processes affecting these surfaces, interpolation across the boundary between the ice shelf and the ice sheet is avoided. Instead, for Antarctica, we first identify all pixels within the ice shelf mask and perform interpolation with all ice sheet pixel information excluded. Subsequently, we identify all pixels within the ice sheet mask and interpolate these separately.

After obtaining two distinct interpolated datasets for the ice shelf and ice sheet, we merge these to produce a single seamless product. This method ensures that the unique characteristics and processes of each surface are accurately represented.

5.3.4.5 Antarctic Pole Hole

In Antarctica, no data exists beyond 88° south, due to the coverage of CryoSat-2. To create a truly seamless product, we must fill this large data gap. We use a basic median calculation to fill the pole hole. After all other interpolation has been completed, we use a pre-defined polygon to isolate pixels adjacent to the pole hole, and calculate the median value of these (to minimise the impact of outlier values). We then fill all pixels in the pole hole with this median value.

5.3.5 Data Sources

Pixels within the final seamless product data can ultimately come from a number of sources. The origin of a pixel is indicated by the 'source' column within the NetCDF file. Table 6 describes each of the five possible sources, gives a description of the processing applied in each case, and lists the regions in which pixels from each source can be found.

Table 6: The different sources of data within the seamless product, and their corresponding 'source' values.

Source ID	Data Source	Description	Zone	Region
0	EOLIS	Calculated by applying RBF gridding to the CryoTEMPO-EOLIS point data.	SARIn	ANT, GRL
1	CRYOTEMPO_LAND_ICE	Calculated by applying RBF gridding to the CryoTEMPO Land Ice point data.	LRM	ANT, GRL
2	KRIGING_INTERPOLATION	Calculated using External Drift Kriging interpolation.	SARIn	ANT, GRL
3	LINEAR_INTERPOLATION	Calculated using linear interpolation.	SARIn and LRM	ANT, GRL
4	MEDIAN_FILL	Calculated by taking the median value of surrounding pixels.	LRM (pole hole only)	ANT

5.3.6 Algorithm Description - Uncertainty Calculation

5.3.6.1 Calculation of Uncertainty Bins

For each gridded pixel in the seamless product, an uncertainty value is calculated using a binning approach, making use of variables associated with the measurement uncertainty.

Firstly, the seamless gridded elevation data is compared to a reference elevation dataset. This is generated by creating an annual DEM from ICESat-2 data, using the same processing technique described in Section 5.3.3.2. This ICESat-2 annual DEM is aligned with the extent of the seamless product, and an elevation difference is calculated for each coincident pixel:

$$\Delta E = E_{seamless} - E_{ICESat-2}$$

As is described for the point uncertainty in Section 4.1.7, the differences ΔE, are made up of many contributing errors, and systematic differences, and thus cannot be directly used as a measure of data uncertainty.

Instead, a binning approach is used to calculate standard deviations of the elevation differences ΔE using bins of roughness and velocity. These are calculated using the reference DEM applied during

the EOLIS processing (ArcticDEM for Greenland, REMA for Antarctica - see Section 4.1.1), and the velocity dataset used during external drift kriging (MEaSUREs Annual Ice Velocity, see Section 5.3.2.1). The roughness is calculated from the reference DEM as the largest difference of a central pixel and its surrounding cells. Clear relationships are visible when comparing both roughness and velocity to the standard deviation of ΔE.

A set of quality bins is generated for each data source described above (EOLIS, CryoTEMPO Land Ice or Linear Interpolation or Kriging). A separate set of quality bins for each data source is necessary as the magnitude of the standard deviation of ΔE varies significantly depending on the data source – it is larger when considering interpolated pixels compared to pixels generated using CryoTEMPO Land Ice data.

Each set of bins is created using all available seamless DEM data that falls within the ICESat-2 time period (2019 – present), and contains an equal volume of data per bin. The number of bins was set to n=40, chosen to balance increasing the precision of the calculated uncertainties with the computational speed of using the bins to assign uncertainties. The bins are generated once, at the start of each new operational Baseline. The standard deviation is calculated from the binned sampled data which gives a range of high to low quality combinations of variables. To ensure that the sample size in each bin is considered, the upper bound of the confidence interval of the standard deviation is calculated:

$$\sigma \leq s\sqrt{\frac{n-1}{\chi^2_{1-\alpha/2}}}$$

where s is standard deviation of the sample, n is sample size, χ^2 is the Chi-square distribution and α is set to 0.05 to give a one-sided 97.5% confidence interval. This upper estimate of the standard deviation is defined as the uncertainty value for each of the quality bin combinations.

Look up tables

The four sets of quality bins are then used as lookup tables (LUT), where each individual gridded elevation measurement is matched to an uncertainty, σ_{TOTAL} , given its roughness and velocity values, and data source:

$$\sigma_{TOTAL} = \begin{cases} \sigma_{EOLIS\ LUT}, if\ source\_id = 0 \\ \sigma_{CLI\ LUT}\ , if\ source\_id = 1 \\ \sqrt{\sigma^2_{EDK\ NTERPOLATED\ LUT} + \sigma^2_{KRIGING}}\ , if\ source\_id = 2 \\ \sigma_{LINEAR\ INTERPOLATED\ LUT}, if\ source\_id = 3 \\ \sqrt{\sigma^2_{LIDAR\ DIFF} + \sigma^2_{MEDIAN\ FILL}}\ , if\ source\_id = 4 \end{cases}$$

For kriging interpolated pixels, the uncertainty generated from the LUT is combined in quadrature with the uncertainty output by External Drift Kriging. It is important to include the kriging uncertainty as it incorporates covariances between each interpolated point and the calibration

points. This error captures both the distance to the nearest calibration data and the local variance for both the observed data and the external drift data sets. As a result, areas of high velocity compared to surroundings have higher uncertainty, and uncertainty increases with distance to the nearest calibration data.

An uncertainty value for pixels within the Antarctic pole hole (source_id = 4) is calculated by combining the standard deviation of the pixels used to calculate the pole hole fill value with the reference estimate of unobserved local variations in elevation. The reference estimate is derived described using airborne lidar measurements, specifically from the 2015/2016 PolarGap campaign (PolarGap, 2018).

In the above equation, $\sigma_{LIDAR\ DIFF}$ is the rounded estimate of unobserved local variations derived from the difference between the interpolated fill value and the lidar elevations for 2015/2016, which is found to be constant at 2m; and $\sigma_{MEDIAN\ FILL}$ is the standard deviation of pixel values contributing to the pole hole median fill for the given year's product.

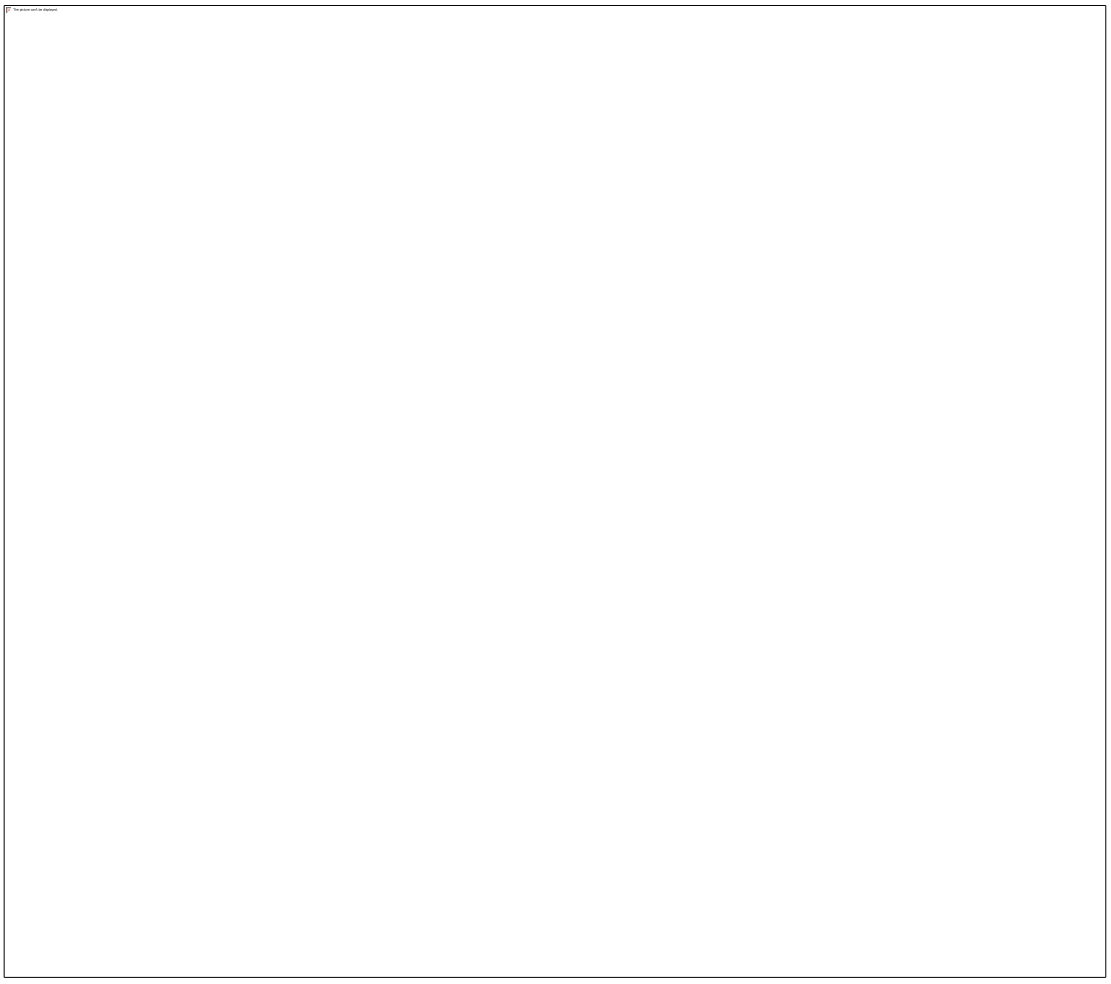

Figure 16: Uncertainty map for an example seamless product (2019), demonstrating the differing uncertainty values for CLI, EOLIS and interpolated pixels.

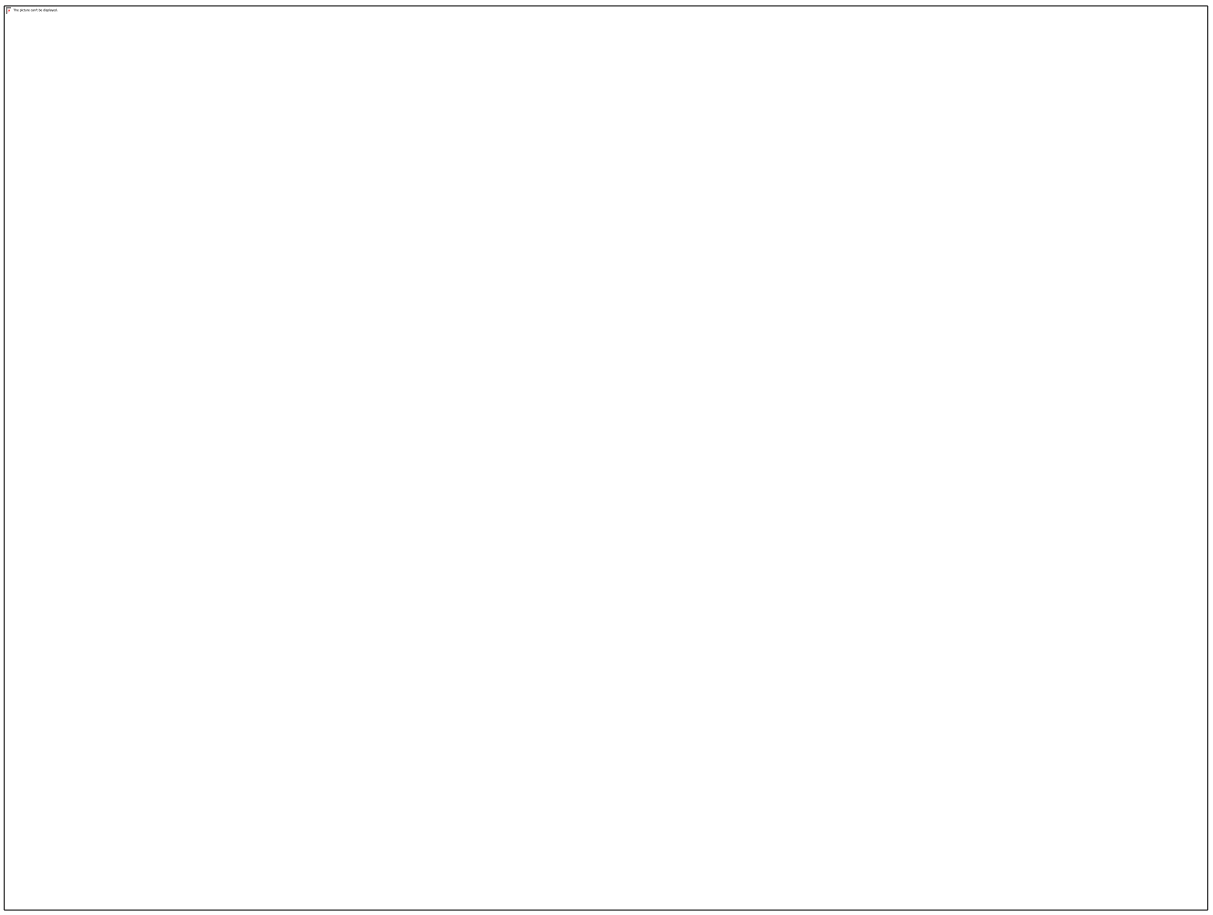

Figure 17: Example of the relationship seen between the difference to ICESat-2 per pixel, and the calculated uncertainties. This is shown per pixel source, where the colour scale shows the volume of pixels that fall into

6 References

Davison, B., Hogg, A., Gourmelen, N., Jakob, N., Wuite, J., Nagler, T., . . . Engdahl, M. (2023). Annual mass budget of Antarctic ice shelves from 1997 to 2021. *Science Advances, 9*(41). doi:https://doi.org/10.1126/sciadv.adi0186

Dong, Y., Zhao, J., Caiyong, L., & Liao, M. (2022). Gapless-REMA100: A gapless 100-m Reference Elevation Model of Antarctica with voids filled by multi-source DEMs. *ISPRS Journal of Photogrammetry and Remote Sensing*.

Dunse, T., Schellenberger, T., Hagen, J. O., Kääb, A., Schuler, T. V., & Reijmer, C. H. (2015). Glacier-surge mechanisms promoted by a hydro-thermodynamic feedback to summer melt. *The Cryosphere, 9*(1), 197-215. doi:10.5194/tc-9-197-2015

ESA. (2019). *CryoSat Baseline D Product Handbook.* Retrieved from https://earth.esa.int/documents/10174/125272/CryoSat-Baseline-D-Product-Handbook

European Space Agency; Sinergise. (2021). Copernicus Global Digital Elevation Model. Retrieved 9 1, 2023, from https://registry.opendata.aws/copernicus-dem

Foresta, L., Gourmelen, N., Pálsson, F., Nienow, P., Björnsson, H., & Shepherd, A. (2016). Surface elevation change and mass balance of Icelandic ice caps derived from swath mode CryoSat-2 altimetry. *Geophysical Research Letters, 43*(12), 138-145. doi:10.1002/2016GL071485

Foresta, L., Gourmelen, N., Weissgerber, F., Nienow, P., Williams, J. J., Shepherd, A., . . . Plummer, S. (2018). Heterogeneous and rapid ice loss over the Patagonian Ice Fields revealed by CryoSat-2 swath radar altimetry. *Remote Sensing of Environment, 211*, 441-455. doi:10.1016/j.rse.2018.03.041

German Aerospace Center (DLR). (2018). TanDEM-X - Digital Elevation Model (DEM) - Global, 90m. doi:10.15489/ju28hc7pui09

Gourmelen, N., Escorihuela, M. J., Shepherd, A., Foresta, L., Muir, A., Garcia-Mondéjar, A., . . . Drinkwater, M. R. (2018). CryoSat-2 swath interferometric altimetry for mapping ice elevation and elevation change. *Advances in Space Research, 62*(6), 1226-1242. doi:10.1016/j.asr.2017.11.014

Gourmelen, N., Goldberg, D., Snow, K., Henley, S., Bingham, R., Kimura, S., . . . Jan van de Berg, W. (2017). Channelized Melting Drives Thinning Under a Rapidly Melting Antarctic Ice Shelf. *AGU, 44*(19), 9796-9804. doi:https://doi.org/10.1002/2017GL074929

Helm, V., Humbert, A., & Miller, H. (2014). Elevation and elevation change of Greenland. *Cryosphere, 8*(4), 1539-1559. doi:10.5194/tc-8-1539-2014

Howat, I. e. (2022). The Reference Elevation Model of Antarctica – Strips, Version 4.1. Harvard Dataverse, V1.

Hugonnet, R., McNabb, R., Berthier, E., Menounos, B., Nuth., C., Girod, L., . . . Kääb, A. (2021). Accelerated global glacier mass loss in the early twenty-first century. *Nature, 592*, 726–731. doi:10.1038/s41586-021-03436-z

Jakob, L., & Gourmelen, N. (2023). Glacier Mass Loss Between 2010 and 2020 Dominated by Atmospheric Forcing. *Geophysical Reseach Letters , 50*(8), 1-10. doi:https://doi.org/10.1029/2023GL102954

Jakob, L., & Gourmelen, N. (2023). Glacier Mass Loss Between 2010 and 2020 Dominated by Atmospheric Forcing. *Geophysical Research Letters, 50*(8), 1-10. doi:10.1029/2023GL102954

Jakob, L., Gourmelen, N., Ewart, M., & Plummer, S. (2021). Spatially and temporally resolved ice loss in High Mountain Asia and the Gulf of Alaska observed by CryoSat-2 swath altimetry between 2010 and 2019. *The Cryosphere, 15*(4), 1845-1862. doi:10.5194/tc-15-1845-2021

Jarvis, A., Reuter, H. I., Nelson, A., & Guevara, E. (2008). *'Hole-filled seamless SRTM data V4', International Centre for Tropical Agriculture (CIAT), available from https://srtm.csi.cgiar.org.*

McMillan, M., Shepherd, A., Gourmelen, N., Dehecq, A., Leeson, A., Leeson, A., . . . Strozzi, T. (2014). Rapid dynamic activation of a marine-based Arctic ice cap. *Geophysical Research Letters, 41*, 8902– 8909. doi:10.1002/2014GL062255

Morlighem, M. (2022). MEaSUREs BedMachine Antarctica, Version 3. *MEaSUREs BedMachine Antarctica, Version 3*. Boulder, Colorado, USA: NASA National Snow and Ice Data Center Distributed Active Archive Center. doi:https://doi.org/10.5067/FPSU0V1MWUB6

Morlighem, M. e. (2022). IceBridge BedMachine Greenland (IDBMG4, Version 5). NASA National Snow and Ice Data Center Distributed Active Archive Center.

Morlighem, M. E., Rignot, T., Binder, D. D., Blankenship, R., Drews, G., & Eagles, O. (2020). Deep glacial troughs and stabilizing ridges unveiled beneath the margins of the Antarctic ice sheet. *Nature Geoscience, 13*, 132-137. doi:https://doi.org/10.1038/s41561-019-0510-8

Padman, L., Erofeeva, S., & Fricker, H. (2008). Improving Antarctic tide models by assimilation of ICESat laser altimetry over ice shelves. *Geophysical Research Letters, 35*. doi:http://dx.doi.org/10.1029/2008GL035592

Padman, L., Fricker, H. A., Coleman, R., Howard, S., & Erofeeva, L. (2002). A new tide model for the Antarctic ice shelves and seas. *Annals of Glaciology, 34*, 247-254. doi:doi:10.3189/172756402781817752

Porter, C., Morin, P., Howat, I., Noh, M.-J., Bates, B., Peterman, K., . . . Nakamura, H. (2018). ArcticDEM, Version 3. *Harvard Dataverse*. doi:10.7910/DVN/OHHUKH

Recchia, L., Scagliola, M., Giudici, D., & Kuschnerus, M. (2017). An Accurate Semianalytical Waveform Model for Mispointed SAR Interferometric Altimeters. *IEEE Geoscience and Remote Sensing Letter, 14*, 1537-1541.

RGI 7.0 Consortium. (2023). Randolph Glacier Inventory - A Dataset of Global Glacier Outlines, Version 7.0. Boulder, Colorado, USA: NSIDC: National Snow and Ice Data Center. doi:doi:10.5067/f6jmovy5navz

RGI Consortium. (2017). Randolph Glacier Inventory - A Dataset of Global Glacier Outlines, Version 6. *NSIDC: National Snow and Ice Data Center*. doi:10.7265/4m1f-gd79

Rignot, E., Velicogna, I., van den Broeke, M. R., Monaghan, A., & Lenaerts, J. T. (2011). Acceleration of the contribution of the Greenland and Antarctic ice sheets to sea level rise. *Geophysical Research Letters, 38*. doi:10.1029/2011GL046583

Slater, T., Lawrence, I. R., Otosaka, I. N., Shepherd, A., Gourmelen, N., Jakob, L., . . . Nienow, P. (2021). Review article: Earth's ice imbalance. *The Cryosphere*, 233–246.

Smith, B., Adusumulli, S., Csathó, B. M., Felikson, D., Fricker, H. A., Gardner, A., . . . ICESAT-2 Science Team. (2021). ATLAS/ICESat-2 L3A Land Ice Height, Version 5. *NASA National Snow and Ice Data Center Distributed Active Archive Center*. doi:10.5067/ATLAS/ATL06.005

Studinger, M. (2014). IceBridge ATM L2 Icessn Elevation, Slope, and Roughness, Version 2. *NASA National Snow and Ice Data Center Distributed Active Archive Center*. doi:10.5067/CPRXXK3F39RV

The IMBIE Team. (2018). Mass balance of the Antarctic ice sheet from 1992 to 2017. *Nature, 558*(7709), 219-222. doi:10.1038/s41586-018-0179-y

The IMBIE Team. (2020). Mass balance of the Greenland Ice Sheet from 1992 to 2018. *Nature, 579*(7793), 233–239. doi:10.1038/s41586-019-1855-2

Wingham, D., Phalippou, L., Mavrocordatos, C., & Wallis, D. (2004). The mean echo and echo cross product from a beamforming interferometric altimeter and their application to elevation measuremen. *IEEE Transactions on Geoscience and Remote Sensing, 40*(10), 2305-2323. doi:10.1109/TGRS.2004.834352

Wouters, B., Gardner, A. S., & Moholdt, G. (2019). Global Glacier Mass Loss During the GRACE Satellite Mission (2002-2016). *Frontiers in Earth Science, 7*. doi:10.3389/feart.2019.00096